Research Square

Preprints are preliminary reports that have not undergone peer review.
They should not be considered conclusive, used to inform clinical practice,
or referenced by the media as validated information.

MyD88 sustains a metastasis-competent cell state by promoting integrin-mediated adhesion in melanoma

Federica Marocchi
European Institute of Oncology
Matteo Lafranconi
European Institute of Oncology
Federico Lazzarini
European Institute of Oncology
Fiorenza Lotti
European Institute of Oncology
Erika Mileti
European Institute of Oncology
Luca Mazzarella
European Institute of Oncology
Laura Furia
European Institute of Oncology
Angelica Zocchi
European Institute of Oncology
Giulia Bertolini
Fondazione IRCCS Istituto Nazionale dei Tumori
Gabriella Sozzi
Fondazione IRCCS Istituto Nazionale dei Tumori
Mario Faretta
European Institute of Oncology
Martin H. Schaefer
European Institute of Oncology
Marine Melixetian
European Institute of Oncology
Luisa Lanfrancone
luisa.lanfrancone@ieo.it

European Institute of Oncology

Research Article

Keywords: Metastasis, melanoma, MyD88, integrin-mediated adhesion, circulating tumor cells (CTCs), endothelial cells, in vivo experimental models

Posted Date: July 3rd, 2026

DOI: https://doi.org/10.21203/rs.3.rs-10118025/v1

License: This work is licensed under a Creative Commons Attribution 4.0 International License. Read Full License

Additional Declarations: No competing interests reported.

Version of Record: A version of this preprint was published at Journal of Experimental & Clinical Cancer Research on October 15th, 2026. See the published version at https://doi.org/10.1186/s13046-026-03853-w.

Abstract

Background. Metastatic dissemination remains a major challenge in melanoma, where environmental cues can reshape tumor cell plasticity and promote transient states that enable cell invasion and colonization of distant organs. However, the tumor cell-intrinsic mechanisms that integrate these external signals and sustain metastatic competence remain incompletely understood.

Methods. To identify tumor cell-intrinsic regulators of melanoma dissemination, we performed functional drop-out screens in NRAS-mutant melanoma patient-derived xenograft (PDX) models. The role of MyD88 was investigated through genetic silencing and overexpression approaches combined with transcriptomic profiling and functional assays of invasion, adhesion, and interaction with endothelial cells and extracellular matrix. Moreover, we carried out *in vivo* metastatic studies and, in particular, extensive circulating tumor cell (CTC) isolation and single-cell analyses. We also evaluated the impact of environmental stimuli on MyD88 expression and downstream signaling pathways.

Results. Functional drop-out screens identify the adaptor protein MyD88 as a tumor cell-intrinsic dependency selectively required for metastatic progression. MyD88 silencing profoundly impairs metastatic dissemination, without affecting primary tumor growth. At the molecular level, MyD88 depletion rewires melanoma cell transcriptional programs, suppressing mesenchymal-like invasive features and reducing metastatic competence. In particular, MyD88 sustains an integrin-mediated adhesion program that enhances tumor cell interactions with the extracellular matrix and endothelium, thereby supporting local invasion, intra- and extravasation and ultimately dissemination to distant sites. Multiple environmental stimuli, including genotoxic stress, growth factors, and nutrient deprivation, increase MyD88 expression and activate STAT3 signaling, which emerges as a central pathway driving integrin-associated adhesive plasticity programs. Within primary tumors, MyD88 identifies a metastasis-competent subpopulation, characterized by pro-adhesive and pro-metastatic transcriptional features. Consistently, circulating tumor cells are enriched for MyD88 expression and display motility- and adhesion-associated states. Conversely, MyD88 interference reduces CTC release and significantly impairs metastatic seeding of distant organs.

Conclusions. These findings establish MyD88 as an environmentally responsive regulator of melanoma cell-state plasticity that links adaptive responses to the acquisition of adhesion-dependent metastatic traits. By coordinating integrin-mediated interactions required for dissemination, MyD88 supports multiple steps of the metastatic cascade.

INTRODUCTION

The development of distant metastases is the principal determinant of poor clinical outcome in melanoma. Despite major clinical advances, a substantial proportion of patients with metastatic melanoma still fail to achieve durable disease control, highlighting the need to better understand the molecular and cellular mechanisms that enable tumor dissemination (1).

A central feature of melanoma progression is non-genetic plasticity, whereby tumor cells dynamically transition between phenotypic programs in response to intrinsic and extrinsic cues (2–4). While classic frameworks described a binary switch between proliferative and invasive states, single-cell profiling has refined this into a continuous transcriptomic spectrum featuring fluid intermediate states (5, 6). Despite this continuum, tumor growth and metastasis appear to be functionally partitioned within a phenotypic hierarchy in which mesenchymal-like cells drive metastatic initiation while contributing minimally to primary tumor growth (7). Notably, dedifferentiated and mesenchymal-like melanoma states are also enriched in lesions refractory to immune checkpoint blockade, suggesting that cellular programs associated with metastatic competence may intersect with therapeutic resistance (8, 9).

Consistent with this view, recent studies have further characterized metastasis-competent subpopulations within primary melanomas and early disseminated compartments, defining distinct molecular programs associated with invasive and disseminating phenotypes. These include PRRX1-associated mesenchymal-like cells, SERPINE2/Protease Nexin1-dependent slow-cycling invasive cells, MCSP-positive metastasis founder cells in sentinel lymph nodes, and GPNMB-positive quiescent cells with pro-metastatic behavior (7, 10–12). Together, these findings indicate that metastatic competence is not a universal property of melanoma cells, but is instead restricted to discrete subpopulations that occupy overlapping, microenvironment-responsive states.

Myeloid differentiation primary response 88 (MyD88) is a core adaptor protein in Toll-like receptors (TLRs) and interleukin-1 receptor signaling, mediating context-dependent downstream responses (13). MyD88 has also been implicated in tumorigenesis through inflammatory signaling within the tumor microenvironment (14, 15) and cancer cell-intrinsic functions across multiple tumor contexts (16–19).

In melanoma, early observations reported TLR4/MyD88 overexpression in human tumor specimens in the broader context of TLR4-driven skin-carcinogenesis (20). Functional evidence later showed that MyD88 knockdown in B16 melanoma cells impairs inflammatory and angiogenic programs and reduces primary tumor growth (21). Beyond primary tumor growth, evidence from a limited number of solid tumor models suggests that MyD88 contributes to aggressive phenotypes associated with invasion and metastatic progression. Consistently, MyD88 silencing impairs migratory and invasive properties in colorectal, mammary, and hepatocellular carcinoma models, and reduces metastatic dissemination (18, 22–24). In melanoma, TLR4-driven signaling has been associated with tumor progression and metastatic dissemination, with MyD88/TRIF-dependent signaling and STAT3 activation emerging as related components of this pathway (25). However, the role of MyD88 as a melanoma cell-autonomous regulator of dissemination and metastatic competence remains insufficiently defined.

Here we identify MyD88 as a selective driver of metastatic progression using an *in vivo* shRNA drop-out screen in metastatic melanoma patient-derived xenografts. MyD88 is dispensable for primary tumor growth but required for efficient dissemination, promoting melanoma cell adhesion to the extracellular matrix and endothelium and thereby facilitating invasion and intra-/extravasation. Mechanistically, MyD88 engages a STAT3-dependent program linked to integrin-mediated adhesion and is required for

melanoma cell plasticity responses to microenvironmental stimuli. Moreover, MyD88 marks a subpopulation within primary melanomas enriched for pro-metastatic features and transcriptionally related to circulating tumor cells. Collectively, these findings identify MyD88 as a melanoma cell-intrinsic mediator of environmental cues, linking them to a STAT3-dependent adhesion program that primes a discrete subpopulation of melanoma cells for ECM remodeling, endothelial interaction, and early metastatic seeding.

MATERIALS AND METHODS

Mice

NOD-SCID-IL2rG null (NSG), C57BL/6, and C3H/He mice aged 4-5 weeks were purchased from Charles Rivers Laboratories and housed in our institutional animal facility at Cogentech (Milan, Italy). Male and female mice aged 7-12 weeks were used for experimental procedures and appropriately randomized across experimental groups. All *in vivo* studies were performed following approval by the institutional animal facility and the Ministry of Health (Institutional Animal Care and Use Committees approvals no. 564/19, 871/20, 565/23 and 442/25), in accordance with the Decreto legislativo 4 marzo 2014, implementing the Directive 2010/63/EU on the protection of animals used for scientific purposes.

Patient-derived xenografts (PDXs), cell lines, and cell treatments

PDXs

Metastatic melanoma patient-derived xenografts (PDXs) were established, propagated and cultured as previously described (26,27). MM13, MM16 and MM23 PDXs at the second *in vivo* passage (PDX2) were maintained in Iscove's Modified Dulbecco's Medium (IMDM, Euroclone, ECB2072) supplemented with penicillin (100 U/mL), streptomycin (100 µg/mL), L-glutamine (2 mM), and 10% fetal bovine serum (FBS, HyClone, SH30071.03).

Cell lines

HEK-293T and A375 cell lines were cultured in Dulbecco's modified Eagle's medium (DMEM, Euroclone, ECM0103L) supplemented with 10% FBS (Euroclone, ECS5000L). SK-MEL3 cell line was cultured in McCoy's 5A medium (Euroclone, ECM0210L) supplemented with L-glutamine (2 mM), and 10% FBS (Euroclone, ECS5000L). WM115 cell line was cultured in Minimum Essential Medium (MEM, Euroclone, ECB2071L) supplemented with L-glutamine (2 mM), 1 mM sodium pyruvate, 0.1 mM non-essential amino acids (NEAA) and 10% FBS (HyClone, SH30071.03). HMEC-1 cell line was cultured in MCDB-131 medium (ThermoFisher, 10372019) supplemented with L-glutamine (2 mM), 10 ng/mL epidermal growth factor (EGF), 1 µg/mL hydrocortisone, and 10% FBS (Euroclone, ECS5000L).

All media were supplemented with penicillin (100 U/mL) and streptomycin (100 µg/mL). All PDXs and cell lines were maintained at 37°C in a humidified incubator with 5% CO_2. All models used in this study were confirmed to be mycoplasma-free before experiments.

In vitro cell treatments

For STAT3 inhibitor (STAT3i) treatment, PDX cells were treated with 500nM BBI608 (Med Chem Express MCE, cat. no. HY-13919) or vehicle control (DMSO) for 4h. For TLR4 inhibitor (TLR4i) treatment, PDX cells were treated with 1μM Resatorvid (Med Chem Express MCE, HY-11109) or vehicle control (DMSO) for 48h. For stimuli treatment experiment, PDX cells were treated with 10mM Temozolomide (TMZ; Sigma Aldrich, T2577), 25ng/ml human TGF-b1 (PeproTech, 100-21C), 3% serum and 3% O2 incubator (Lows) for 24h.

For MyD88-overexpression experiment, transduced PDX cells and melanoma cell lines were maintained in medium supplemented with tetracycline-free fetal bovine serum (Euroclone, ECS01182L) and induced with doxycyclin (Sigma-Aldrich, D9891) at the following concentrations: MM13, 25ng/ml; MM16, 100ng/ml; SK-MEL3 50ng/ml; WM115, 10ng/ml for 24h.

Plasmids

shRNA constructs

shRNAs targeting human or murine MyD88 were synthesized (Sigma-Aldrich) and cloned into the pRSI17-U6-(sh)-UbiC-TagGFP-2A-Puro vector, linearized vector (Cellecta, SVSHU617-L), according to the manufacturer's instructions. Two independent shRNA sequences were generated for each gene, individually validated and subsequently pooled during lentiviral production for cell transduction. A luciferase-targeting shRNA (**shLuc**) and a non-targeting scramble shRNA (**shSCR**) were used as control where indicated. The shRNA sequences are listed in the **Supplementary Table 7**.

MyD88 expression vector

The human MYD88 coding sequence (NM_002468.5) was cloned into the doxycycline-inducible Tet-On lentiviral vector pCW57.1 (Addgene, 41393) to generate pCW57.1-MyD88. The pCW57.1 backbone was linearized by double digestion with NheI and AgeI, and together with the amplified MyD88 insert, was purified using the QIAquick PCR Purification Kit (Qiagen, 28106) and assembled using NEBuilder HiFi DNA Assembly (New England Biolabs, E2621) according to the manufacturer's instructions. Correct insertion of the MyD88 coding sequence was confirmed by Sanger sequencing.

Lentiviral production and cell transduction

Lentiviral particles were produced in HEK293T cells by co-transfection of transfer vectors with the second-generation packaging plasmids pMD2.G-VSV-G and pCD-NLBH (gift from Prof. Colin Goding, Ludwig Cancer Research, Oxford, UK). Transfection was performed using Lipofectamine LTX/PLUS Reagent Kit for shRNA libraries (Invitrogen) or the calcium phosphate method for single-shRNA vectors. Target cells were transduced in complete medium supplemented with polybrene (Sigma-Aldrich) at MOI 3–4 for validation experiments. Medium was replaced after 16 h, and transduced cells were selected with puromycin for 3 days.

In vivo experiments

In vivo metastasis genetic screen and data analysis

Two custom barcoded libraries were generated by chip-based oligonucleotide synthesis and cloned as pooled libraries into the pRSI16-U6-(sh)-UbiC-TagRFP-2A-Puro lentiviral vector (Cellecta). The non-targeting (NT) library consisted of 1,200 barcoded vectors, each carrying a unique barcode and no associated shRNA. The targeting library contained 874 barcoded vectors targeting 77 candidate genes and 4 positive-control genes (PSMA1, RPL30, PCNA, POLR2B), with 10 shRNAs *per* gene to ensure redundancy (**Supplementary Table 1**).

MM13 and MM16 PDX cells were transduced with the libraries at a multiplicity of infection (MOI) of 0.3 to achieve a final library coverage of at least 275x. A total of 1,000,000 transduced cells were collected as pre-injection reference sample. For *in vivo* screen, 330,000 cells *per* mouse were resuspended in a 1:3 (v/v) mixture of Matrigel Matrix HC (Corning, 354248) and L-15 medium (Sigma Aldrich, L5520) and injected intradermally in the back of anesthetized NSG mice. Primary tumors were surgically resected at 300 mm^3 and metastatic organs were collected when mice reached humane endpoint criteria.

Genomic DNA from reference samples was extracted using Blood & Tissue Kit (Qiagen, 69506), according to manufacturer's instruction. Genomic DNA from tumor and metastatic organs was extracted using phenol-chloroform protocol after tissue homogenization in gentleMACS M tubes (Miltenyi Biotec, 130-093-236) in P1 buffer (50mM Tris-HCl pH 8.0, 10mM EDTA, RNAse A 100µg/ml) supplemented with SDS.

Barcode cassettes were PCR-amplified and sequenced by next-generation sequencing according to the Cellecta user manual, with optimizations to enable sample multiplexing. PCR products were purified using the QIAquick PCR Purification Kit (Qiagen, 28106), quality-controlled using High Sensitivity DNA Assay on an Agilent 2100 Bioanalyzer and sequenced on Illumina HiSeq-2000 or NovaSeq-6000. Sequencing reads were processed and analyzed using an in-house pipeline, as previously described(26,27).

For the NT-library feasibility screen, detected barcodes (reads³1) were enumerated per sample, normalized to total aligned reads, and compared across primary tumors and metastases using log2 fold-change distributions.

In the targeting-library analysis, genes were classified as hits when ≥50% of their associated barcodes were undetected and ≥60% of the remaining detected barcodes were depleted. Depleted barcodes were defined as those with a log2 fold change below the median of the log2 fold-change distribution across all detected barcodes. This analysis was adapted from previously described approaches (analysis adapted from (26,27)).

In vivo screen validation

PDXs and cell lines were transduced with control or shMyD88 constructs and injected intradermally into anesthetized recipient mice (MM13, MM16, 300,000 cells per NSG mouse, SW1 200,000 cells per C3H mouse, and B16-BL6 500,000 cells per C57BL/6 mouse). Primary tumors were monitored by caliper measurement and surgically resected at 300 mm³. After resection, mice were euthanized at day 90 or followed for Kaplan–Meier survival analysis. At endpoint, lungs and livers were collected, FFPE-processed, sectioned, and H&E-stained to assess metastatic burden.

In vivo colonization assay

MM13 shLuc- and shMyD88-transduced cells were resuspended in PBS and injected into the tail vein of NSG mice (1×10^6 cells per mouse in 100 µL of PBS). Mice were euthanized 50 days after injection. Lungs and livers were formalin-fixed, paraffin-embedded and stained for human nuclei (Sigma-Aldrich, MAB-4383) by immunohistochemistry; human nuclei-positive signal was quantified using **QuPath** software.

In vivo competition extravasation assay

MM13 cells were separately transduced with shSCR-RFP or shMyD88-GFP constructs. Cells were mixed at a 1:1 ratio and the input ratio was verified by flow cytometry before injection (T0 reference). Cell mixtures were resuspended in PBS and injected into the tail vein of NSG mice (1×10^6 shSCR-RFP plus 1×10^6 shMyD88-GFP cells *per* mouse). Mice were euthanized 7 days after injection, and lungs and livers were collected. Organs were mechanically dissociated, using gentleMACS Tissue Dissociator in enzymatic dissociation medium containing collagenase IV (Gibco, 17104-019) and dispase (STEMCELL technologies, 07913). Single-cell suspensions were subjected to erythrocyte lysis with ACK Lysing Buffer (Gibco, A10492-01), filtered, stained with Live/Dead Fixable Blue 510 viability dye (BD Biosciences; #564408), and fixed in 1% paraformaldehyde before FACS acquisition (BD FACSCelesta). Flow cytometry data were analyzed using FlowJo software. GFP-positive, RFP-positive and double-negative populations were quantified among live single cells. Organs from non-injected mice were used as negative controls.

Circulating tumor cells (CTC) isolation and quantification

MM13 shLuc- and shMyD88-transduced cells were injected intradermally into anesthetized NSG mice (300,000 cell *per* mouse). Whole blood was collected by cardiac puncture when primary tumors reached 300 mm³ or 800 mm³, approximately 28 and 38 days after injection, respectively. Blood was collected in 10% EDTA and subjected to erythrocyte lysis using **BD** lysing buffer (BD, 555899) at a 1:10 ratio for 10 min at room temperature. After washing, cell pellets were resuspended with AutoMACS Buffer (autoMACS® Rinsing Solution Rinsing Solution, 130-091-222, supplemented with 0.5% BSA) and incubated with Mouse Cell Depletion Microbeads (Miltenyi, 130-104-694) and Anti-Ter 119 MicroBeads (Miltenyi, 130-049-901) for 15min **at 4 °C**.Samples were then washed, resuspended in autoMACS Buffer and processed on an **autoMACS Pro Separator** using the **DepleteS** program. Human CTCs were enriched in the negative fraction. Enriched samples containing **GFP-positive CTCs** were imaged using an **Incucyte live-cell analysis system** (Sartorius), and quantified by direct fluorescence-based counting.

Multiplex protein immunofluorescence of primary tumor sections

FFPE primary tumor sections from untransduced, shLuc- and shMyD88-transduced MM13 tumors collected at 300 mm^3 were processed using the Multiple Interactive Labelling by Antibody Neodeposition (MILAN) workflow(28). Briefly, sections (5 µm) were deparaffinized, rehydrated and subjected to heat-induced antigen retrieval in Tris-EDTA buffer (pH 8). After permeabilization with 0.5% Triton X-100 and blocking with 5% BSA, slides were incubated overnight at 4 °C with primary antibodies against MyD88 (rabbit; Abcam, ab133739), Ki67 (mouse IgG1; BD, 558616), PCNA (Rat; ChromoTek, 16d10), ITGAV (mouse IgG2a; BioLegend, 327907), ITGA5 (rabbit; Chemicon, AB1928), ITGB3 (mouse IgG1; BioLegend, 336407), CD44 (rabbit; Abcam, ab157107), Lamin A (mouse IgG3; Invitrogen, MA1-06101), and followed by fluorophore-conjugated secondary antibodies (detailed in **Supplementary Table 7**) and DAPI counterstaining. All the primary antibodies were used at a concentration of 10 ug/ml. The detection fluorophore for each channel was chosen according to the level of expression of each marker of interest in order to maximize the signal-to-noise ratio over the autofluorescence background present in the visible light range. Near-infrared channel was dedicated in every step to the detection of Lamin A control target to monitor that antigen accessibility was maintained and sample structural integrity (**Supplementary table 7**). After each imaging round, antibodies were removed using an SDS/β-mercaptoethanol-based stripping buffer, and slides were re-stained for subsequent antibody cycles.

Multichannel fluorescence images were acquired on a Nikon Ti2 inverted microscope equipped with a Crest X-Light V3 spinning-disk confocal module, Lumencor Celesta laser source and Photometrics Kinetix camera, controlled by NIS-Elements software v6.10.02. Sequential imaging was performed using custom NIS-Elements JOBs and ImageJ routines (29). Low-resolution maps were acquired with a 10×/0.45 objective for tissue mapping and repositioning across staining rounds, followed by high-resolution confocal single-plane imaging with a 60×/1.4 NA oil-immersion objective. Sequential images were registered on the DAPI channel using ImageJ v1.54j. Single-cell image cytometry was performed with the A.M.I.CO pipeline (30). Nuclei were segmented from DAPI, cell boundaries were defined using CD44 signal and Voronoi tessellation, and fluorescence intensities were extracted from all channels. Lamin-A-low objects, segmentation artifacts and area/circularity outliers were excluded. Mean fluorescence intensity per pixel was used for downstream analyses. High- and low-expressing cells were defined by Gaussian fitting of the lower intensity distribution and thresholding at the upper full-width half-maximum. For spatial analyses, gated cells were binned by normalized marker expression, and the distance between each bin barycenter and the tissue-section barycenter was calculated.

Bulk RNA sequencing

Bulk RNA sequencing was performed on MM13 shLuc- and shMyD88-transduced primary tumors resected at 300 mm^3. Total RNA was extracted using Quick RNA Miniprep (Zymo Research) according to manufacturer's instructions, and RNA integrity was assessed using an Agilent 2100 Bioanalyzer with RNA 6000 Nano Chip Kit. RNA-sequencing libraries were generated starting from 1 µg of total RNA with TruSeq RNA sample preparation kit v2 (Illumina, 15025063), following the manufacturer's instructions,

quality-controlled using the **High Sensitivity DNA Assay** on an Agilent 2100 Bioanalyzer, and sequenced as 50-bp paired-end reads on a NovaSeq 6000 System (Illumina).

Host mouse reads were removed using Xenome(31), and remaining reads were aligned to the human genome using TopHat2 version 2.0.9. Gene-level counts were generated with HTseq(32), and differential expression analysis was performed using DESeq2 Bioconductor package(33).

Differentially expressed genes between shMyD88 and shLuc conditions were identified using a negative binomial generalized linear model with absolute log2 fold-change values >1 and adjusted p values <0.05. Gene Ontology and pathway enrichment analyses were performed using **DAVID v6.8 (34,35)**and**Enrichr (36,37).**

TCGA dataset correlation analysis

Gene expression data for skin cutaneous melanoma from the TCGA-SKCM dataset (n=469) were downloaded from GDC data portal (https://portal.gdc.cancer.gov/projects/TCGA-SKCM). Z-scores for individual genes were calculated as $Z = (x - \mu) / \sigma$, where x represents the expression value of a given gene in a specific sample, μ represents the mean expression of that gene across all samples, and σ represents the standard deviation. Gene set expression z-scores were calculated as $S_j = 1/\sqrt{k} \sum_{i=1} z_{ij}$, where k is the total number of genes included in the specific signature and z_{ij} is the calculated Z-score of the i-th gene in the signature for sample j. Correlation between MyD88 expression and gene set expression z-scores for selected human gene sets were calculated using Spearman correlation.

***In vitro* functional assays**

Matrix-adhesion assay

Twelve-well plates were coated with fibronectin (Roche, 11080938001, 15 μg/ml in PBS) for 2h at 37°C. PDX cells were seeded at 30,000 cells per well, and non-adherent cells were removed by PBS washing after 20 min for MM13 and 45 min for MM16. Adherent cells were imaged using an EVOS microscope.

2D transwell invasion assay

Transwell inserts (24-well format, 8μm pore size; Corning, 353097) were coated with rat-tail type I collagen (Corning, 354249, 2mg/ml). Cells were seeded in the upper chamber (30,000 cells in 200 μl serum-free IMDM), with 800 μl IMDM supplemented with 10% FBS in the lower chamber. After 24 h, non-invading cells were removed from the upper membrane surface with cotton swabs, and invaded cells on the lower membrane surface were stained with 0.5% crystal violet, imaged on an EVOS microscope and quantified using ImageJ software.

3D spheroids invasion assay

PDX cells were cultured as hanging drops in 20μl medium containing 0.2% methylcellulose (R&D Systems, HSC001) (1,000 cells per droplet). After 72h, aggregated cell spheroids were embedded in 70

µl serum-free collagen matrix (1.5 mg/ml for PDX shLuc/shMyD88, SKMEL3 and WM115 CTR/oeMyD88; 3 mg/ml for PDX CTR/oeMyD88) in 96-well plates and polymerized for 1h at 37 °C. Complete medium (140µl) was then added, supplemented where appropriate with: doxycycline (MM13, 100ng/ml; MM16, 400ng/ml; SKMEL3/WM115, 500ng/ml), BBI608 (50-100nM), cilengitide 1mM or stimuli (TMZ, 20 mM, TGFb, 50 ng/ml, 3% serum 3% O2). Spheroids were imaged at 0, 24h (PDX) and 72h (SKMEL3/WM115) using an EVOS microscope, and invasion area was quantified with ImageJ by manually outlining the invasion front and normalizing to time 0.

For RNA extraction, spheroids were collected, after collagenase IV digestion (Gibco, 17104-019; 1mg/ml), and RNA was extracted using the PicoPure RNA Isolation Kit (Applied Biosystems, 12204).

For time-lapse experiments, spheroids were embedded in collagen in Ibidi 8-well chamber slides (GmbH) and imaged on a Leica SP8 AOBS Lightning confocal microscope. Images were acquired every 30 min for 15 h using a 20× objective and 45 plans with a 2 µm step size. Analysis was performed using the Manual Tracking plugin in Fiji.

3D spheroids viability assay

PDX spheroids were generated and embedded in collagen as described above. Complete medium containing the indicated BBI608 concentrations was added on top of the polymerized matrix. Cell viability was assessed at 24h using the CellTiter-Glo 3D Cell Viability Assay (Promega, G9681), according to the manufacturer's instructions.

Tumor-endothelial adhesion assay

HMEC-1 cells were seeded in 24-well plates (250,000 cell/well) and allowed to adhere overnight (16h). After medium removal, PDX cells were seeded (150,000 cells/well) on top of the endothelial monolayer. After 2h, non-adherent cells were removed by PBS washing, and adherent cells were imaged using an EVOS microscope.

Transendothelial-migration assay

HMEC-1 cells were seeded on 24-well transwell inserts (Corning, 353097, 30,000 cells per transwell) and cultured for 16 h to form an endothelial monolayer. PDX cells were then plated on top of the monolayer (200,000 cells/transwell in 200 mL serum-free IMDM), with 800 ml complete IMDM in the lower chamber. After 36h, non-migrated cells were removed with cotton swabs, and migrated cells on the lower membrane surface were imaged using an EVOS microscope and quantified with ImageJ.

For cell collection, the assay was scaled to 6-well transwell inserts format, using 400,000 HMEC-1 cells and 1.2 x 10^6 PDX cells *per* insert. Non-transmigrated cells were recovered from the upper compartment, whereas transmigrated cells were trypsinized from the lower membrane surface. Both fractions were then processed for RNA extraction.

Angiogenic endothelial cell tube formation assay

Forty-eight-well plates were coated with growth factor-reduced Matrigel (Corning, 356231) and incubated for 30min at 37 °C to allow polymerization. HMEC-1 cells were resuspended in PDX-conditioned medium collected after 72h of culture and seeded on top of the Matrigel layer (80,000 cells per well). After 8h, tube formation was imaged using an EVOS microscope, and angiogenic parameters were quantified with the Angiogenesis Analyzer macro for Fiji/ImageJ.

DAMPs release detection

PDX cells were treated with the indicated stimuli, and culture supernatants were collected after 48h. Secreted HSP70/HSPA1A levels were measured using the DuoSet ELISA kit (R&D Systems/Bio-Techne, DY1663-05), extracellular ATP using the **CellTiter-Glo Luminescent CellViability Assay** (Promega, **G7570)** and HMGB1 using the Lumit HMGB1 Immunoassay(Promega, W6110), according to the manufacturers' instructions. Concentrations were calculated using a four-parameter logistic (4-PL) curve fit and normalized to cell number at the end of treatment.

MyD88$^{high/low}$ FACS sorting and RNA extraction

MM13 and MM23 PDX melanoma cells from primary tumors were used to sort MyD88-high and MyD88-low subpopulations, starting from 30 million cells. Cells were washed in PBS, fixed and permeabilized using the Cytofix/Cytoperm Plus Kit (BD, 554715), according to the manufacturer's instructions. After washing, cells were incubated with anti-MyD88 primary antibody (Abcam, ab133739; 1:200) for 20 min at room temperature, followed by PE-conjugated anti-rabbit IgG secondary antibody for 20 min at room temperature. Doublets were excluded by FSC-H versus FSC-A gating, and debris was excluded based on FSC-A versus SSC-A scatter properties. MyD88^{high} and MyD88^{low} cells, corresponding to the upper and lower 10% of the MyD88-PE fluorescence distribution, respectively, were then sorted and collected using a BD FACSMelody cell sorter (Becton Dickinson).

RNA was extracted from sorted cells using the RNeasy FFPE Kit (Qiagen, 73504), according to the manufacturer's instructions. Reverse transcription and qPCR were performed as described above.

FACS analysis of integrin expression

MM13, MM16 and MM23 PDX cells (1 × 10⁶ cells *per* sample) were stained with Fixable Viability Stain 510 (BD Biosciences, 564406; 1:1,000) for 15 min at room temperature. After washing, cells were incubated with anti-ITGAV antibody (CD51; PE/Cy7; BioLegend, 327915) and anti-ITGB3 antibody (CD61; Alexa Fluor 647; BioLegend, 336407) for 30 min on ice. Cells were then fixed and permeabilized (as described above), incubated with anti-MyD88 primary antibody (Abcam, ab133739; 1:200) for 20 min at room temperature, followed by Alexa Fluor 555-conjugated anti-rabbit secondary antibody (1:400) for 30 min at room temperature. Samples were acquired on a Cytek Aurora full-spectrum flow cytometer (Cytek Biosciences) using SpectroFlo® software for spectral unmixing, and data were analyzed using FlowJo

software (v10, BD Biosciences). The gating strategy was applied hierarchically: debris was excluded based on FSC-A versus SSC-A scatter properties, doublets were excluded by FSC-H versus FSC-A gating, and dead cells were excluded by gating on Fixable Viability Stain 510-positive events. MyD88-high and MyD88-low populations were defined among live single cells as described above, and integrin-positive cells were identified using negative controls.

Single-cell RNA sequencing and analysis

MM13 cells were injected intradermally into NSG mice (300,000 cells *per* mouse). At tumor volumes of 300mm³ and 800mm³, CTCs were isolated from whole blood as described above, and matched primary tumors were mechanically dissociated into single-cell suspensions.

Primary tumor cells and CTCs were counted, resuspended in 0.04% BSA/PBS according to 10x Genomics guidelines, and processed using Chromium Next GEM Single Cell 3' Reagent Kit v3.1 (10x Genomics). Libraries were sequenced on a NovaSeq 6000 platform (Illumina) to a target depth of 50,000 reads *per* cell. Sequencing output was demultiplexed into FASTQ files using Illumina bcl2fastq, and barcode processing and single-cell 3' gene counting were performed with Cell Ranger v6.0.1. cDNA reads were aligned simultaneously to the GRCh38 human and GRCm39 mouse reference genomes. Cells were retained if >90% of reads associated with valid barcodes and UMIs mapped confidently to human genome. Doublets and multiplets were removed using *scDblFinder* (38). Quality control was performed by retaining cells with >300 detected genes per cell and <10% mitochondrial UMI counts. To maintain a balanced representation of primary tumor and CTC samples in downstream analyses, tumor samples were downsampled to 1,500 cells *per* sample, yielding a final dataset of 7,652 cells. Data normalization and integration were performed with Seurat v4.1 package with the RPCA method. Principal component analysis was used for dimensionality reduction, and Louvain clusters generated from a k-nearest neighbor graph were subsequently merged based on hierarchical clustering dendrogram to define the final clusters, which were visualized by UMAP embeddings.

Marker genes for each cluster were identified using *FindAllMarkers* function with the Wilcoxon rank-sum test. For primary tumor clusters, the top 200 marker genes ranked by adjusted P value were used for Gene Ontology analysis with DAVID, using the GO Biological Process 2025 annotation. Additional enrichment analyses for cluster 7 and for MyD88-positive versus MyD88-negative tumor cells were performed using Reactome 2024, Panther 2016, MSigDB Hallmark 2020 and NCI-Nature gene sets.

Gene expression distribution plots and dot plots were generated using log-normalized SCT-transformed expression values. MyD88-positive cells were defined using a threshold of ≥1 MyD88 read.

Trajectory and pseudotime analyses were performed using Monocle2 package (39). Trajectories were inferred by first reducing dimensionality using the Discriminative Dimensionality Reduction with Trees algorithm implemented in the DDRTree R package v. 0.1.5 (https://github.com/cole-trapnell-lab/DDRTree). Cells were ordered without specifying a predefined root state or the number of terminal cell states, according to the unsupervised dpFeature procedure.

RNA extraction and quantitative RT-PCR

Total RNA was extracted using the Quick-RNA MiniPrep (Zymo Research, ZYR1055), and cDNA was synthesized using the OneScript Plus cDNA synthesis kit (abm, G236), according to the manufacturers' instructions. Quantitative RT-PCR was performed using Fast-SYBR Green Master mix (Applied Biosystem, 4385614) on the C1000 Thermal Cycler (Bio-Rad). Each reaction contained 20ng (6 µl) cDNA, 10µl SYBR Green Master Mix and 4µl of 2µM forward/reverse primer mix. Amplification was performed at 95 °C for 2min, followed by 40 cycles of 95°C for 10s and 60°C for 30s. Relative gene expression was calculated using the 2−ΔΔCt method and normalized to RPLP0 expression. The qPCR primer sequences are listed in the **Supplementary Table 7**.

Western Immunoblot

PDX cells were lysed in RIPA Buffer (Tris-HCl 50mM, NaCl 150mM, 1% NP-40, 0.5% Sodium Deoxylcholate, 0.1% SDS) supplemented with protease (Roche, 11697498001) and phosphatase (ThermoScientific, A32957) inhibitor cocktails. After sonication, protein concentration was determined using Bradford reagent (Bio-Rad). Heat-denatured proteins were separated on 8–12% SDS-PAGE gels and transferred onto nitrocellulose membranes. Membranes were blocked in 5% non-fat milk or 5% BSA in TBST and incubated overnight at 4 °C with primary antibodies against: MyD88 (abcam, ab133739), phospho-STAT3 (Tyr705) (Cell Signaling, 9145), total STAT3 (Cell Signaling, 9132), phospho-P65 (Ser536) (Cell Signaling, 3033), total P65 (Cell Signaling, 8242); vinculin (Sigma, cat. no. V9131) was used as loading control. After washing, membranes were incubated with HRP-conjugated secondary antibodies, and chemiluminescent signals were acquired using a ChemiDoc Imaging System (Bio-Rad).

Statistical analysis and reproducibility

Data are presented as mean ± standard deviation (SD) unless otherwise indicated. Statistical analyses and graphs were generated using GraphPad Prism 10.6.0. Sample sizes, replicate numbers and statistical tests are reported in the corresponding figure legends. $P < 0.05$ was considered statistically significant. In vitro experiments were performed with at least 3 independent biological replicates. Samples, cells and mice were randomly allocated to experimental groups when applicable.

RESULTS

Genetic drop-out screen identifies melanoma metastasis driver genes

To identify genes driving melanoma dissemination *in vivo*, we established a model of spontaneous metastasis using two NRAS-mutant metastatic melanoma patient-derived xenografts (PDXs), MM13 and MM16, derived from cases selected from our previously characterized melanoma patient cohort(26). Following orthotopic intradermal injection of PDX cells into NSG mice and subsequent surgical resection of primary tumors at 300 mm^3, we observed extensive dissemination to axillary and inguinal lymph nodes, lungs and liver (**Fig. 1a**). Overall, metastatic spread was detected in the vast majority of mice

(100% and 88% in the MM13 and MM16 models, respectively), with quantitative differences in organ involvement across the two models. MM13 displayed a broader metastatic pattern, with metastases detected in a higher proportion of mice across all three analyzed sites than in MM16, while both models showed a relative preference for lymph node colonization over visceral organs (**Fig. 1b**, **Supplementary Fig. 1a-b**).

To assess the feasibility of an *in vivo* genetic drop-out screen for metastasis in these two models, PDX cells were transduced with a non-targeting (NT) library containing 1,200 uniquely barcoded plasmids without associated shRNAs(27) prior to *in vivo* injection. Barcode complexity was quantified by next-generation sequencing (NGS) in reference cells (pre-injection), primary tumors (n=3) and metastatic organs (MM13, n=8; MM16, n=7; **Fig. 1c**, **Supplementary Fig. 1c**). Primary tumors retained complete NT barcode representation relative to the reference library, while metastatic organs showed preserved library complexity with an average barcode recovery of 98.1% relative to the injected library (range: 92.2–100% across samples) (**Fig. 1d**). The log2-transformed ratio between individual BC reads in each metastasis and the matched primary tumor followed a symmetric distribution, with an overall median of 0 across pooled samples, and only a modest narrowing of barcode repertoire complexity in lung lesions (**Fig. 1e**; **Supplementary Fig. 1d**). The BCs comparable representation between primary tumors and matched metastases demonstrates that the drop-out screen is a feasible approach to characterize metastasis dynamics in these two PDX models.

Next, we conducted a drop-out screen in these two PDXs using a pooled shRNA library targeting 77 genes(27) (10 shRNAs *per* gene; **Supplementary Table 1**). Primary tumors and available matched metastases were collected from both models (MM13, n=3 primary tumors, n=4 metastases; MM16, n=3 primary tumors, n=8 metastases; **Fig. 1f**, **Supplementary Fig. 1e**) and shRNA-barcode depletion was quantified. To specifically capture dissemination-associated dependencies, shRNA-barcode depletion in metastases was assessed relative to matched primary tumors, thereby controlling for the primary tumor growth effect. Depleted genes were identified using a two-criteria approach, requiring that at least 50% of their barcodes were undetected and that at least 50% of the detected barcodes were depleted (**Fig. 1g**). After defining the candidate-gene set for each metastatic lesion (**Supplementary Table 2**), we quantified pairwise similarity across samples using the Jaccard index, based on the overlap between screen-identified candidate genes. This analysis showed limited overlap across lesions, with an overall mean Jaccard index of 0.31 (**Fig. 1h**). Consistently, most candidate genes were detected in only one or two samples, whereas progressively fewer hits were shared by three or four lesions (**Fig. 1i**), revealing a heterogeneous landscape of metastatic dependencies.

We then compared dependencies across lesions from both PDXs and identified a core set of ten shared metastatic candidates (**Fig. 1j**). This set included genes belonging to melanoma-relevant pathways, such as MAPK signaling (BRAF, KRAS, RAF1), PI3K–AKT signaling (AKT3, PIK3CB, PIK3C2B), cell-cycle regulation (CCNE1), developmental signaling (NOTCH2), matrix remodeling (MMP2), and signaling mediators (MYD88). Whereas all other candidates were also recovered as dependencies for primary tumor growth (**Supplementary Table 3**), MyD88 shRNA-barcodes were not depleted in primary tumors,

indicating that MyD88 is dispensable in this setting but may instead be selectively required for metastasis. MyD88 encodes an adaptor protein downstream of Toll-like and interleukin-1 receptors, yet its cell-autonomous role in melanoma dissemination remains poorly defined, making it a compelling candidate for further investigation.

Feasibility assessment of the drop-out screen (**c-e**). **c.** MM13 and MM16 PDX cells were transduced with a barcoded (BC) non-targeting library (1,200 BC complexity) and injected intradermally into NSG mice (330,000 cells/mouse; n=3 *per* PDX). Primary tumors (n=3) and metastatic organs (MM13, n=8; MM16, n=7) were collected as reported above. **d.** Number of detected non-targeting barcodes (reads ≥ 1) in MM13 and MM16 reference (transduced cells, Ref), primary tumors (PT) and metastatic organs (LN, lung, liver). **e.** Average distribution of log2 fold-change (FC) of BC frequencies in metastatic organs, relative to PT (10^{th} to 90^{th} percentile of read count data are reported).

Drop-out screen with targeting shRNA library (77 genes, 10 shRNA-BCs/gene; **f-j**). **f.** MM13 and MM16 PDX cells were transduced with the targeting library (874 BCs complexity) and injected intradermally into NSG mice (330,000 cells/mouse; n=3 *per* PDX). Primary tumors (n=3) and metastatic organs (MM13, n=4; MM16, n=8) were collected as reported above. **g.** Identification of candidate genes from the screen by a two-criteria analysis based on the number of undetected BCs and the percentage of depletion of detected BCs; the dashed lines indicate thresholds. **h.** Jaccard index matrix showing the similarity among individual metastatic samples based on shared candidate genes across the two PDX models. **i.** Bar plot showing the number of shared hits across MM13 and MM16 (LNs and non-LNs) samples. **j.** Venn diagram of exclusive and shared hits across MM13 LN, MM16 LN and MM16 non-LN, defined as genes detected in at least two samples *per* group.

MyD88 drives an invasive transcriptional program targeting cell adhesion properties

To validate the contribution of MyD88 to melanoma dissemination, we silenced MyD88 using two pooled shRNAs, both of which had been previously verified to effectively knock down MyD88 expression (**Supplementary Fig. 2a**). We orthotopically injected control (shLuc) or MyD88-silenced (shMyD88; **Supplementary Fig. 2b**) MM13 cells into NSG mice. Following primary tumor resection, we monitored the mice for dissemination as previously described. The two groups showed comparable primary tumor growth rates (**Fig. 2a-b**, **Supplementary Fig. 2c**), consistent with unmodified protein expression of the proliferation marker Ki67 in tumor sections (**Fig. 2c**), together with sustained MyD88 silencing (**Supplementary Fig. 2d**).

Conversely, MyD88 knockdown profoundly impaired metastatic dissemination. At 90 days post-injection, we observed a significant reduction in lymph node involvement, in terms of both the number and volume of metastatic LNs (**Fig. 2d**), as well as in the extent of metastatic foci in the lungs and liver (**Fig. 2e**). This translated into significantly prolonged mice overall survival as determined by Kaplan-Meier analysis, with median survival increasing from 82 to 117 days (**Fig. 2f**). This phenotype, characterized by unchanged primary tumor growth kinetics coupled with significantly prolonged survival, was corroborated in the MM16 PDX model (**Supplementary Fig. 2e-g**; **Fig. 2g**). We further validated these findings in two highly

invasive syngeneic murine models: NRAS-mutant SW1 and BRAF/NRAS wild-type B16-BL6. In both instances, MyD88 depletion resulted in a greater than two-fold increase in survival (**Supplementary Fig. 2h-o**), indicating that the requirement for MyD88 in metastatic progression is conserved beyond the PDX setting and is maintained in immunocompetent hosts.

To investigate the molecular mechanism underlying this phenotype, we analyzed the transcriptional profile of shLuc and shMyD88 primary tumors by bulk RNA sequencing. Despite comparable growth rates (**Fig. 2a**), primary tumors were overall extensively reprogrammed at the transcriptional level upon MyD88 knock-down. The top ranking differentially downregulated genes following MyD88 silencing were linked to extracellular matrix remodeling and stromal interactions (LRRC15, FIBIN*, SPOCK, HAS2, GREM1, PDGFB*), adhesion/motility and neural-like programs (*ICAM1, CNTN1, GAS7, SCN2A, GABRA3, SOX4, RUNX1T1*), and inflammatory mediators (*CXCL1, TNFSF8, XAF1*) (**Supplementary Fig. 2p**). The full set of significantly downregulated genes in shMyD88 versus shLuc tumors (48 genes; Log2FC < -1, adjusted p < 0.05; **Supplementary Table 4**) was strongly enriched for genes associated with previously described invasive, neural-crest like, and AXL-high melanoma cell states (**Fig. 2h;** WIMMS Database(40)). Consistently, functional annotation of these genes highlighted categories related to epithelial-to-mesenchymal transition (EMT), cell adhesion, extra cellular matrix (ECM) organization, TGF-β signaling, and integrins-mediated interactions (**Fig. 2i**).

Notably, STAT3 signaling emerged as the main pathway among the enriched categories associated with the MyD88-dependent downregulated programs. Accordingly, MyD88 silencing attenuated STAT3 activation, reflected by reduced phospho-STAT3 Tyr705, whereas NF-κB (p65), a canonical mediator of MyD88 signaling, remained unaffected (**Fig. 2j**).

Having identified a MyD88-dependent invasive and adhesion-associated transcriptional program, we extended this analysis to MM16 and to a third NRAS-mutant PDX, MM23(26), included for independent functional validation. Consistent with the most prominently regulated functional categories, shMyD88 cells derived from all three PDX models exhibited broad and concordant downregulation of EMT-like and metastasis-associated genes, adhesion molecules and integrins, known to mediate melanoma cell adhesion to both ECM and endothelial cells(41) (**Fig. 2k**, **Supplementary Fig. 2q**).

MyD88 drives metastasis by promoting cell adhesion to extracellular matrix and endothelium

Tumor cell adhesion to the ECM facilitates detachment and relocation from the primary site, whereas interaction with endothelial cells is required for intravasation and subsequent dissemination, representing critical early steps of metastatic cascade(42). Consistent with this model, we found that MyD88 depletion directly impairs these early dissemination-associated processes. In MM13 cells MyD88-silencing reduced adhesion to fibronectin by 47% (**Fig. 3a**; validated in MM16, **Supplementary Fig. 3a**) and decreased invasion through collagen matrices by 43% (**Fig. 3b**). Furthermore, real-time 3D spheroid invasion assays confirmed that MyD88 knockdown severely restricts **spheroid cell invasion**, resulting in diminished cell velocity and cumulative distance traveled **(Fig. 3c; Supplementary Fig. 3b).**

Because interaction with endothelial cells is a prerequisite for intravasation and subsequent colonization of secondary sites, we next investigated whether MyD88 regulates this critical step of the metastatic cascade. MyD88-silenced MM13 cells exhibited a 55% reduction in adhesion to dermal microvascular endothelial cells (HMEC-1) (**Fig. 3d**), a phenotype also observed in the MM16 and MM23 PDX models (**Supplementary Fig. 3c**). Using an *in vitro* trans-endothelial assay, we found that MyD88 silencing significantly reduced MM13 transmigration across the endothelial barrier (**Fig. 3e**), a phenotype consistently observed across our additional PDX models (**Supplementary Fig. 3d**). Since MyD88 signaling is known to regulate the expression of cytokines, chemokines, and pro-angiogenic mediators, we next investigated whether soluble factors secreted by PDX cells contribute to endothelial remodeling. To this end, endothelial cells were exposed to conditioned media derived from shLuc or shMyD88 cells. Conditioned media from shMyD88 cells impaired the angiogenic tube-forming capacity of endothelial cells compared to control conditioned media derived from shLuc cells, as reflected by reduction in the main parameters of endothelial network formation, including the number of nodes, junctions, segments, and meshes (**Fig. 3f**). These findings provide supportive evidence that, beyond regulating tumor cell-intrinsic properties, MyD88 may also contribute to tumor-endothelial crosstalk through secreted factors, thereby shaping a permissive endothelial context.

Taken together, these findings suggest that MyD88-silenced tumors may have an altered intravasation efficiency which translates in a reduced number of circulating tumor cells (CTCs) *in vivo*. To address this, MM13 shLuc and shMyD88 cells were orthotopically injected, and whole blood was collected at two defined tumor stages, corresponding to tumor volumes of 300 mm^3 and 800 mm^3 (28 and 38 days, respectively; 48 total mice; **Fig. 3g**). Following immunomagnetic depletion of murine blood components and enrichment of human melanoma cells, CTCs were efficiently isolated and quantified based on GFP positivity (see Materials and Methods). In line with our previous observations (**Fig. 2a**), MyD88 silencing did not affect primary tumor growth throughout the experiment (**Supplementary Fig. 3e-f**). In contrast, while CTC counts in shLuc tumors remained stable across the two time points (approximately 30–48 cells/ml blood), MyD88 silencing significantly reduced CTCs release at both time points by 63% and 90%, respectively (**Fig. 3h**).

Since successful metastatic colonization depends on efficient extravasation and early seeding at distant sites, we next assessed the contribution of MyD88 to these processes *in vivo*. NSG mice were intravenously injected with a 1:1 mixture of control shSCR-RFP and shMyD88-GFP MM13 cells (**Fig. 3i**; **Supplementary Fig. 3g-h**), and the relative abundance of tumor cells in the lungs and liver was quantified based on RFP/GFP signal (**Fig. 3j**). At 7 days post-injection, shSCR cells markedly outcompeted shMyD88 cells, with mean shSCR:shMyD88 proportions of 81.0:19.0% in the lungs and 80.5:19.5% in the liver, consistent with impaired extravasation and early metastatic seeding upon MyD88 silencing (**Fig. 3j**; **Supplementary Fig. 3i**). This early competitive disadvantage translated into a profound reduction in metastatic colonization at later time points. Fifty days post-injection, lymph node metastases were detected in 80% of shLuc-injected mice, whereas no lymph node involvement was observed in the shMyD88 group. Likewise, metastatic burden in distant organs was markedly reduced, decreasing on average by 73.6% in the lungs and 96.2% in the liver compared with controls (**Fig. 3k**).

Environmental cues amplify a MyD88–STAT3 pro-invasive program in melanoma

Given that MyD88 silencing attenuated the invasive phenotype, we next asked whether enforced MyD88 expression was sufficient to drive melanoma invasiveness. Using a doxycycline-inducible system, we achieved physiologically relevant MyD88 overexpression (approximately 3- to 4-fold over baseline) in our PDX models (**Fig. 4a**; **Supplementary Fig. 4a,** first lane). MyD88 induction increased the expression of EMT-associated genes and integrins in MM13 and MM16 PDX cells (**Fig. 4a**; **Supplementary Fig. 4a**), resulting in enhanced invasion of 3D spheroids derived from both metastatic models (**Fig. 4b**; **Supplementary Fig. 4b-c**)**.** Notably, MyD88 overexpression was also sufficient to promote invasiveness even in poorly invasive melanoma models, such as SK-MEL3 and WM115 melanoma cells (**Supplementary Fig. 4d-e**)**.**

We next assessed the involvement of the STAT3 pathway in downstream signaling, as its activity was reduced upon MyD88 silencing (**Fig. 2i**). MyD88 overexpression enhanced STAT3 signaling relative to control cells, while NF-κB signaling remained unaffected (**Fig. 4c**; **Supplementary Fig. 4f-g**), consistent with our previous observations (**Fig. 2i**). Interestingly, pharmacological inhibition of STAT3 with BBI608, at concentrations that did not affect cell viability (**Supplementary Fig. 4h**), restored phospho-STAT3 levels in MyD88-overexpressing cells to basal levels comparable to those of control cells (**Fig. 4c**) Moreover, BBI608 preferentially impaired the invasive capacity of MyD88-overexpressing spheroids relative to control spheroids (**Fig. 4d**), indicating that the pro-invasive phenotype driven by MyD88 is functionally dependent on STAT3 signaling. Consistently, STAT3 inhibition reduced the expression of EMT-associated genes and integrins previously linked to the MyD88-dependent phenotype (**Fig. 2j-4a**; **Fig. 4e**), further supporting the existence of a STAT3-dependent transcriptional program downstream of MyD88. To investigate the contribution of integrin-mediated adhesion, we next targeted integrin $\alpha V\beta 3$ using the selective antagonist cilengitide. Notably, cilengitide markedly reduced invasion in MyD88-overexpressing spheroids while exerting minimal effects under control conditions (**Fig. 4f**), highlighting an increased reliance on integrin-dependent adhesive signaling in the context of MyD88-driven invasion.

To investigate whether MyD88 expression is modulated by microenvironmental signals, we first examined its association with established environmental stress-response signatures. In addition to the expected correlation with STAT3 signaling, used here as a positive control, MyD88 expression also showed moderate-to-strong correlation with DNA damage/repair, TGF-β signaling, and hypoxia pathways (**Supplementary Fig. 4i**). Accordingly, exposure of MM13 and MM16 cells to a panel of environmental stressors, including temozolomide (TMZ, genotoxic stress/ DNA damage), TGF-β, and nutrient- and oxygen -deprived conditions (low-oxygen/low-serum, Lows), induced MyD88 upregulation relative to untreated controls, by 4.6-, 1.5- and 2.7-fold, respectively (**Fig. 4g**, **Supplementary Fig. 4j**). Notably, in both PDXs these stimuli also induced the expression of *VEGF, MMP2, ITGA5, ITGAV,* and *ITGB3,* collectively defining a transcriptional program associated with melanoma plasticity and invasion (**Supplementary Fig. 4k-l**). While robust induction of these genes was observed in shLuc cells (approximately 2-11-fold depending on the stimulus and target gene), this response was consistently

attenuated in MyD88-silenced cells (**Fig. 4h**, **Supplementary Fig. 4m**), indicating that MyD88 is required for environmentally induced adaptive and invasive transcriptional reprogramming.

Accordingly, these environmental stimuli promoted 3D spheroid invasion in control cells (**Supplementary Fig. 4n**)**, increasing invasion by 32%, 22%, and 15% under TMZ,** TGF-β **and** low-oxygen/low-serum **conditions, respectively, whereas this effect was markedly reduced upon MyD88 silencing (Fig. 4i). Likewise, pharmacological inhibition of STAT3 abrogates stimulus-induced invasion (Fig. 4j), indicating that environmentally driven invasive behavior** depends on **the MyD88-STAT3 axis.**

Finally, we found that exposure to these stimuli promoted the release of damage-associated molecular patterns (DAMPs), including HMGB1, HSP70, ATP (**Fig. 4k**). Given the established ability of these DAMPs to engage TLR4 and activate downstream signaling pathways, we next investigated the contribution of TLR4 to the TMZ-induced response. Pharmacological inhibition of TLR4 using resatorvid markedly attenuated the effects induced by TMZ treatment (**Supplementary Fig. 4o**), suggesting that DAMP-mediated TLR4 signaling might contribute to the adaptive response triggered by genotoxic stress.

MyD88 identifies a pro-metastatic sub-population within the primary tumor

Given the strong association between MyD88 signaling and invasive phenotype observed in our functional studies, we next asked whether endogenous heterogeneity in MyD88 expression within primary tumors could identify melanoma cell populations with distinct invasive features. Immunophenotypic analysis of PDX-derived primary tumor cells revealed heterogeneous MyD88 expression, enabling the isolation of $MyD88^{high}$ and $MyD88^{low}$ subpopulations from MM13 and MM23 tumors by FACS sorting (top and bottom 10% of MyD88-expressing cells, respectively) (**Fig. 5a**, **Supplementary Fig. 5a**). $MyD88^{high}$ cells exhibited approximately 1.5-fold higher MyD88 expression relative to $MyD88^{low}$ cells and concomitantly displayed increased expression of invasive-associated markers, including *TGFB1, AXL,* and *PDGFRB* (**Fig. 5a**, **Supplementary Fig. 5a**). To assess the spatial localization of $MyD88^{high}$ cells and their association with structural, proliferation, and adhesion markers, we performed multiplexed high resolution confocal image cytometry on immunostained MM13 tumor sections (**Supplementary Fig. 5b**). This approach was designed to exploit the advantages of a diffraction limited spatial resolution in optically sectioned images. Analysis of the spatial distribution of $MyD88^{high}$ cells showed that they were not enriched within specific tumor regions, but rather broadly dispersed throughout the tumor mass. Consistently, no statistically significant differences were observed relative to Lamin A, used as a reference marker (**Supplementary Fig. 5c**). In contrast, although $MyD88^{high}$ and $MyD88^{low}$ cells displayed comparable levels of the proliferation markers Ki67 and PCNA, $MyD88^{high}$ cells showed increased expression of the adhesion-related markers ITGAV, ITGA5, ITGB3 (**Fig. 5b, Supplementary Fig. 5b**). Consistently, across three PDXs (MM13, MM16, and MM23), $MyD88^{high}$ cells contained a higher fraction of ITGAV+ITGB3+ cells than $MyD88^{low}$ cells (**Fig. 5c**), indicating increased expression of the functionally active integrin heterodimer $\alpha V\beta 3$. Reciprocally, ITGAV+ITGB3+ cells expressed higher levels of MyD88 across all PDX models analyzed (**Supplementary Fig. 5d**).

To functionally assess the role of MyD88 expression in the early steps of the metastatic cascade, we performed an *in vitro* trans-endothelial assay with MM13 cells. Non-transmigrated and transmigrated cells were separately collected from the upper and lower compartments, respectively. Transmigrated cells exhibited increased expression of MyD88, together with established intravasation markers (APP, ADAM12, MCAM) and integrins (ITGA5, ITGAV, ITGB3) (**Fig. 5d**), delineating a subpopulation characterized by an intravasation-associated, pro-adhesive transcriptional program.

We next evaluated the role of MyD88 in the context of *in vivo* tumor cell dissemination and CTC release. Following orthotopic injection of MM13 cells, CTCs were collected, together with their matched primary tumors, at two distinct tumor stages, corresponding to primary tumor volumes of 300 mm^3 and 800 mm^3, respectively (**Fig. 3g**), and subjected to single-cell RNA sequencing (scRNAseq). After quality-control filtering, the dataset comprised 7,650 high-quality melanoma cells, including 7,000 primary tumor cells and 650 CTCs across the two tumor stages. Single cell transcriptomes were clustered and visualized by UMAP-based dimensionality reduction (**Fig. 6a**; **Supplementary Fig. 6a**). Unsupervised trajectory inference revealed that primary tumors comprised multiple coexisting subpopulations, whereas CTCs followed a more ordered and linear trajectory, consistent with a more defined evolutionary process (**Supplementary Fig. 6b-c**). Despite being collected at early and advanced stages of tumor growth, primary tumors displayed remarkably similar cluster distributions. This pattern highlights the heterogeneous cellular architecture of these lesions, including clusters associated with DNA replication, mitosis, differentiation, ER/metabolism, translation, and signaling (**Supplementary Fig. 6d**; **Supplementary Table 5**). In contrast, CTCs displayed a highly homogeneous transcriptional identity and were predominantly enriched in cluster 7 (**Fig. 6b**). Notably, cluster 7 displayed increased expression of MyD88, integrin/adhesion signatures, and STAT3 pathway activation compared to the other clusters (**Fig. 6c**). In particular, cluster 7 cells were enriched for pathways related to extracellular matrix organization and degradation, angiogenesis and EMT (**Fig. 6d**; **Supplementary Table 5**), further supporting the association of CTCs to the metastatic process.

We next extended the analysis beyond cluster composition by directly comparing primary tumors and CTCs collected at both tumor burdens. Because single-cell RNA-seq primarily resolves cell states based on transcript detectability rather than precise quantitative expression levels in the individual cells, MyD88+ and MyD88– cells were used as proxies for $MyD88^{high}$ and $MyD88^{low}$ populations, respectively. Within this framework, CTCs showed an approximately 2-fold increase in the proportion of MyD88+ cells relative to primary tumors (mean 52% versus 28%, respectively; **Fig. 6e**). This enrichment was accompanied by increased expression of MyD88 itself, together with the pro-adhesive integrins ITGAV and ITGB3 in CTCs compared with primary tumor cells (**Fig. 6f-h**).

Having established that $MyD88^{high}$ cells display invasive features and are enriched within the circulating tumor cell compartment, we next investigated how these cells relate to defined transcriptional states within the primary tumor. To this end, we identified marker genes of MyD88+ cells relative to the remaining tumor cell populations (**Supplementary Table 6**), indeed including several invasion- and matrix remodeling- associated genes, such as COL6A1, COL6A2, CTSL, CTSD, SERPIN2, GPNMB, and TIMP1.

Pathway analysis showed that these cells shared a transcriptional program overlapping with cluster 7, characterized by enrichment of extracellular matrix organization/degradation, integrin signaling, and angiogenesis pathways (**Fig. 6i**). Direct comparison with MyD88- cells further demonstrated increased activation of integrins, adhesion, and STAT3 pathways within the MyD88+ population (**Fig. 6j**). In addition, MyD88+ cells showed strong similarity to previously described AXL, invasive, and neural crest-like transcriptional states (**Supplementary Fig. 6e**). Consistently, trajectory analysis revealed that MyD88+ cells within primary tumors were preferentially enriched in late pseudotime states relative to MyD88- cells, while the circulating compartment was similarly skewed toward this late pseudotime region (**Fig. 6k**). Together, these findings indicate that CTCs occupy a cellular state closely resembling the MyD88+ invasive subpopulation identified within the primary tumor.

In conclusion, these data suggest that MyD88 identifies a pre-existing subpopulation within primary tumors with pro-metastatic features, which is functionally equipped for dissemination and is enriched during tumor progression (**Fig. 7**).

DISCUSSION

Metastatic progression remains the leading cause of melanoma-related mortality and a persistent clinical challenge. Despite substantial clinical advances driven by immune checkpoint blockade and emerging cellular therapies, many patients with advanced melanoma still experience therapy resistance, disease progression, and limited durable benefit (1, 43, 44). However, the mechanisms and dependencies underlying tumor cell dissemination are only partially understood (45). This unmet need is particularly evident in NRAS-mutant melanoma, where direct NRAS-targeted strategies remain investigational and approved genotype-directed options are still limited (46, 47).

Recent work has defined melanoma dissemination as cell-state dependent process shaped by tumor-cell plasticity and microenvironmental inputs. Single-cell studies have shown that melanoma cells occupy a continuum of melanocytic, intermediate, and mesenchymal-like states, rather than discrete phenotypic identities. Functional studies indicate that primary tumor growth and metastatic dissemination are not sustained uniformly across this continuum, but can be driven by distinct subpopulations (5–7). These programs are additionally shaped by spatial and microenvironmental cues, including tissue architecture, mechanical constraints, and organ-specific signals, which can remodel tumor cell phenotypes and influence metastatic competence (11, 48, 49). Therefore, the key unresolved question is which tumor-cell-intrinsic regulators translate environmental inputs into dissemination-competent behavior *in vivo*.

Addressing this question requires experimental systems that capture the metastatic cascade in its complexity. Orthotopic and spontaneous-metastasis models are particularly valuable in this regard, as they preserve tissue context, natural routes of dissemination, and clinically relevant interactions with extracellular matrix and vascular interfaces more effectively than simplified experimental-metastasis models (50, 51). In this context, patient-derived spontaneous metastasis models provide a valuable framework to study dissemination within a physiologically relevant *in vivo* setting and to causally

interrogate tumor cell programs required for metastatic competence (52). More broadly, metastatic dependencies are not adequately resolved by descriptive profiling alone, but require *in vivo* functional approaches. In particular, although prior *in vivo* RNA-interference screens have provided important insights into metastatic regulators, many relied on experimental metastasis models that capture only selected steps of the cascade, or on drop-in strategies that identify metastasis suppressors rather than genes required for dissemination itself (53–59). Loss-of-function drop-out screening strategies remain relatively uncommon, with few recent examples reported in ovarian and breast cancer (60, 61), and are particularly scarce in melanoma, where only one drop-out screen has been reported (62).

Using an *in vivo* functional drop-out approach suited to capture metastatic dependencies in a heterogeneous process, we identify MyD88 as a tumor cell-intrinsic regulator of melanoma dissemination. Although a few studies in other tumor types had associated MyD88 with invasion and metastasis (18, 22–24), the evidence remained limited and mechanistically unresolved. In melanoma, upstream MyD88-associated signaling has been implicated in disease progression, but a selective and autonomous requirement of tumor cells for MyD88 in spontaneous dissemination and maintenance of metastasis-competent status has not been clearly established (63, 64).

Our results demonstrate that MyD88 silencing does not affect primary tumor growth but instead profoundly alters downstream transcriptional programs linked to metastatic fitness, supporting the view that dissemination can depend on selective state-specific programs that do not necessarily confer a proliferative advantage within the primary lesion. In this context, the MyD88-driven invasive phenotype appears to rely primarily on adhesion-dependent dissemination. Adhesion molecules promote tumor cell interactions with extracellular matrix components, including laminins, collagens, fibronectin and vitronectin, as well as with counter-receptors such as ICAM and VCAM on vascular endothelial cells. Increased adhesive capacity is a recognized determinant of metastatic progression, facilitating local invasion, intravasation, vascular arrest, transendothelial migration and colonization of distant sites (41, 42).

Prior studies in other tumor types suggested that upstream stimulation of TLR4/MyD88-related signaling can converge on integrin-dependent adhesive phenotypes (65–67). However, our work extends these observations by showing that, in melanoma, MyD88 itself acts as a tumor cell-intrinsic regulator of a coordinated program of integrin-dependent adhesion that functionally converges on dissemination.

Mechanistically, our findings indicate that MyD88 sustains an adhesion program enriched for integrin-linked and αVβ3-associated functions through STAT3-dependent axis. This is consistent with coordinated modulation of MyD88 and STAT3 expression, as well as with the ability of STAT3 inhibition to phenocopy MyD88 loss. Our results also refine the interpretation of downstream signaling. Although MyD88 classically signals through NF-κB, particularly in inflammatory settings (68), its tumor-cell-autonomous pro-invasive functions have been linked to multiple downstream pathways across cancer models, including PI3K/AKT, p38/ERK, NF-κB, and Snail-driven EMT signaling (23, 24). In melanoma, TLR4-MyD88 outputs have been shown to engage both NF-κB-linked invasive pathways (63, 69, 70) and a

distinct STAT3-associated arm (25). Our data therefore indicate that, in our models, MyD88-dependent dissemination is more tightly coupled to STAT3-dependent adhesion than to canonical NF-κB activity.

Recent work has shown that melanoma metastatic competence is dynamically shaped by microenvironmental cues, including mechanical confinement at the tumor-stroma interface, IFNγ-driven remodeling of nodal founder cells, and organ-specific metabolic milieus that bias metastatic tropism (11, 48, 49). In this context, the MyD88-driven adhesive phenotype appears to be part of a broader plasticity program responsive to environmental cues. In our system, genotoxic stress, growth factor stimulation, and nutrient deprivation induced MyD88 expression and promoted invasive and adhesion-associated responses, whereas MyD88 silencing markedly attenuated these adaptive phenotypes. Together, these findings suggest that MyD88 is not merely a static marker, but a functional mediator that translates environmental inputs into a dissemination-relevant program that supports metastatic progression.

We found that MyD88 is broadly yet heterogeneously expressed within the primary tumor. Notably, the MyD88^{high} fraction is enriched for pro-metastatic transcriptional features and displays a greater propensity to intravasate. Because such metastasis-competent states are expected to represent rare and plastic populations within the primary tumor, we specifically designed complementary approaches to isolate and profile them, including FACS-based separation of endogenous MyD88^{high} and MyD88^{low} cells and analysis of cells selected by trans-endothelial migration. Since CTCs represent the immediate output of intravasation and an obligate, yet rare, intermediate of metastatic spread, we made dedicated efforts to isolate and profile low-abundance CTCs from PDX-bearing mice, allowing direct single-cell comparison with matched primary tumor cells. This analysis revealed an enrichment of MyD88-positive cells within the circulating compartment, supporting the idea that the MyD88-driven program is relevant along the actual dissemination trajectory. Transcriptomic studies of melanoma CTCs from patients and experimental models have highlighted metastatic competence-associated programs, including cellular motility, invasiveness, and WNT5A/SPARC-associated mesenchymal features (71, 72). Only a limited number of studies have identified more specific CTC-associated programs, such as RPL/RPS-associated translational remodeling linked to brain metastasis progression and transferrin-dependent lipogenic and iron-homeostasis pathways (73, 74). However, whether MyD88-associated signaling contributes to this CTC-related metastatic program in melanoma has not been directly addressed. Previous studies identified enrichment of MyD88-associated signaling in ovarian cancer CTCs, although these observations were descriptive and did not establish a causal role for MyD88 in CTC formation (75). Likewise, integrin programs have been linked to CTC-associated metastatic behavior in breast cancer, without evidence supporting a role for MyD88 (76).

Importantly, functional perturbation studies in our models indicate that the link between MyD88 expression and metastatic dissemination extends beyond a purely correlative association. Genetic silencing of MyD88 markedly reduced CTC release, compromised transendothelial migration and extravasation-associated fitness, and ultimately impaired metastatic colonization. Collectively, these data position MyD88 as a functional regulator of a dissemination-competent tumor cell state that arises

within the primary tumor, is transcriptionally related to circulating tumor cells, and becomes selectively enriched during metastatic progression.

These findings are consistent with the emerging paradigm that metastatic competence in melanoma is encoded within specialized tumor cell states, which have been variably described across studies as mesenchymal-like dissemination programs, slow-cycling invasive populations, rare metastasis-initiating cells, or quiescent pro-metastatic states (7, 10–12). Our work extends this framework by identifying MyD88 as a functional determinant of a dissemination-competent melanoma cell state that actively enables metastatic progression. In particular, our data position MyD88 at the intersection of adhesion-associated metastatic fitness and CTC generation, linking microenvironmental responsiveness through STAT3 signaling to the execution of adhesion-dependent dissemination programs. Together, these findings identify a MyD88–STAT3-driven cellular program that promotes cell dissemination during melanoma metastatic progression.

Abbreviations

CTC, Circulating Tumor Cell; DAMP, Damage-Associated Molecular Pattern; ECM, Extracellular Matrix; EMT, Epithelial-to-Mesenchymal Transition; FACS, Fluorescence-Activated Cell Sorting; FFPE, Formalin-Fixed Paraffin-Embedded; GO, Gene Ontology; H&E, Hematoxylin and Eosin HMEC, Human Microvascular Endothelial Cell; IHC, Immunohistochemistry; LN, Lymph Node; MOI, Multiplicity of Infection; MyD88, Myeloid Differentiation Primary Response 88; NF-κB, Nuclear Factor Kappa B; NSG, NOD-SCID IL2Rγnull; PDX, Patient-Derived Xenograft; RNA-seq, RNA Sequencing; RT-qPCR, Reverse Transcription Quantitative Polymerase Chain Reaction; scRNA-seq, Single-Cell RNA Sequencing; TGF-β, Transforming Growth Factor Beta; TMZ, Temozolomide; UMAP, Uniform Manifold Approximation and Projection.

Declarations

Ethics approval and consent to participate

This study complied with all ethical regulations regarding animal experimentation. The use of animals was approved by the institutional animal facility and the Ministry of Health (Institutional Animal Care and Use Committees approvals no. 564/19, 871/20, 565/23 and 442/25), in accordance with the Decreto legislativo 4 marzo 2014, implementing the Directive 2010/63/EU on the protection of animals used for scientific purposes. Additionally, tissue biopsies of metastatic melanomas were collected from patients whose informed consent was obtained in writing according to the policies of the Ethics Committee of the European Institute of Oncology and regulations of the Italian Ministry of Health. The studies were conducted in full compliance with the Declaration of Helsinki (26).

Consent for publication

All the authors have read and approved the final manuscript and consent to its publication.

Availability of data and materials

Gene expression datasets generated in this study are publicly available in the Gene Expression Omnibus (GEO) at GSE335241. Confidential access for peer review has been enabled through GEO using the reviewer link and token provided: GEO reviewer link: https://www.ncbi.nlm.nih.gov/geo/query/acc.cgi?&acc=GSE335241; Reviewer token: udqpeuwixtmnxmj

Competing interests

The authors declare that they have no competing interests.

Funding

This work was supported by the Associazione Italiana per la Ricerca sul Cancro (AIRC IG 28890 to LL) to LL and the Italian Ministry of Health with Ricerca Corrente and 5x1000 funds. F.M. was supported by Fondazione Umberto Veronesi (2023-2024-2025-2026) fellowships. F.L. is a PhD student registered in the PhD Program in Systems Medicine, established by the University of Milan in collaboration with the European School of Molecular Medicine (SEMM).

Author contributions

Conceptualization: F.M., L.L.; Methodologies: F.M., M.L., F.L., Fi.L., E.M., L.M., L.F., A.Z., G.B., G.S., M.F., M.M.; Data Curation and Computational Analysis: F.M., M.F., M.M., M.S.; Resources: L.L.; Writing – original draft: F.M., L.L.; Writing – review and editing: all authors; Supervision: L.L.; Funding Acquisition: L.L.

Acknowledgements

The authors wish to thank the IEO Genomic Unit and Simona Ronzoni (IEO Flow Cytometry Unit) for their considerable technological support, and Alberto Gobbi and Manuela Capillo from Cogentech (Milan, Italy) for their excellent assistance in mouse work. We are especially grateful to Daria Duca for collecting and providing organ tissues for histological staining, Lorenzo Ciacci for insightful discussions on the mechanistic aspects of the study, Giovanna Jodice for histological staining of tissue samples, Massimo Barberis for expert pathological support in the interpretation of histological and immunohistochemical data, and Francesco Tucci for analytical support.

References

1. Robertson BM, Fane ME, Weeraratna AT, Rebecca VW. Determinants of resistance and response to melanoma therapy. Nat Cancer. 2024;5:964–82.
2. Hoek KS, et al. In vivo switching of human melanoma cells between proliferative and invasive states. Cancer Res. 2008;68:650–6.

3. Rambow F, Marine JC, Goding CR. Melanoma plasticity and phenotypic diversity: Therapeutic barriers and opportunities. Genes Dev. 2019;33:1295–318.
4. Arozarena I, Wellbrock C. Phenotype plasticity as enabler of melanoma progression and therapy resistance. Nat Rev Cancer. 2019;19:377–91.
5. Tirosh I, et al. Dissecting the multicellular ecosystem of metastatic melanoma by single-cell RNA-seq. Sci (1979). 2016;352:189–96.
6. Wouters J, et al. Robust gene expression programs underlie recurrent cell states and phenotype switching in melanoma. Nat Cell Biol. 2020;22:986–98.
7. Karras P, et al. A cellular hierarchy in melanoma uncouples growth and metastasis. Nature. 2022;610:190–8.
8. Pozniak J, et al. A TCF4-dependent gene regulatory network confers resistance to immunotherapy in melanoma. Cell. 2024;187:166–e18325.
9. Pozniak J, Marine JC. Decoding melanoma's cellular mosaic to unlock immunotherapy potential. Trends Cell Biol. 2025;35:911–21.
10. Perego M, et al. A slow-cycling subpopulation of melanoma cells with highly invasive properties. Oncogene. 2018;37:302–12.
11. Guetter S, et al. MCSP+ metastasis founder cells activate immunosuppression early in human melanoma metastatic colonization. Nat Cancer. 2025;6:1017–34.
12. Lotti F, et al. GPNMB marks a quiescent cell population in melanoma and promotes metastasis formation. EMBO Rep. 2025;26:3804–30.
13. Medzhitov R, et al. MyD88 is an adaptor protein in the hToll/IL-1 receptor family signaling pathways. Mol Cell. 1998;2:253–8.
14. Rakoff-Nahoum S, Medzhitov R. Regulation of spontaneous intestinal tumorigenesis through the adaptor protein MyD88. *Science (1979).* 317, 124–127 (2007).
15. Swann JB et al. Demonstration of inflammation-induced cancer and cancer immunoediting during primary tumorigenesis. *Proc. Natl. Acad. Sci. U. S. A.* 105, 652–656 (2008).
16. Coste I, et al. Dual function of MyD88 in RAS signaling and inflammation, leading to mouse and human cell transformation. J Clin Invest. 2010;120:3663–7.
17. Treon SP, et al. MYD88 L265P Somatic Mutation in Waldenström's Macroglobulinemia. N Engl J Med. 2012;367:826–33.
18. Zhu G, et al. MyD88 mediates colorectal cancer cell proliferation, migration and invasion via NF-κB/AP-1 signaling pathway. Int J Mol Med. 2020;45:131–40.
19. Liu J et al. MyD88's function in the emergence and growth of tumors. Clin Cancer Bull 3, (2024).
20. Mittal D, et al. TLR4-mediated skin carcinogenesis is dependent on immune and radioresistant cells. EMBO J. 2010;29:2242–52.
21. Trucco LD, et al. Downregulation of adaptor protein MyD88 compromises the angiogenic potential of B16 murine melanoma. PLoS ONE. 2017;12:1–18.

22. Egunsola AT, et al. Growth, metastasis, and expression of CCL2 and CCL5 by murine mammary carcinomas are dependent upon Myd88. Cell Immunol. 2012;272:220–9.
23. Liang B, et al. Myeloid differentiation factor 88 promotes growth and metastasis of human hepatocellular carcinoma. Clin Cancer Res. 2013;19:2905–16.
24. Jia RJ, et al. Enhanced myeloid differentiation factor 88 promotes tumor metastasis via induction of epithelial-mesenchymal transition in human hepatocellular carcinoma. Cell Death Dis. 2014;5:1–10.
25. Fu XQ, et al. Activation of STAT3 is a key event in TLR4 signaling-mediated melanoma progression. Cell Death Dis. 2020;11:1–15.
26. Bossi D, et al. In Vivo genetic screens of patient-derived tumors revealed unexpected frailty of the transformed phenotype. Cancer Discov. 2016;6:650–63.
27. Marocchi F, et al. Actionable Genetic Screens Unveil Targeting of AURKA, MEK, and Fatty Acid Metabolism as an Alternative Therapeutic Approach for Advanced Melanoma. J Invest Dermatology. 2023;143:1993–e200610.
28. Hu M, Coleman S, Judson-Torres RL, Tan AC. The classification of melanocytic gene signatures. Pigment Cell Melanoma Res. 2024;37:854–63.
29. Hamidi H, Ivaska J. Every step of the way: Integrins in cancer progression and metastasis. Nat Rev Cancer. 2018;18:533–48.
30. Chastney MR, Kaivola J, Leppänen VM, Ivaska J. The role and regulation of integrins in cell migration and invasion. Nat Rev Mol Cell Biol. 2025;26:147–67.
31. Boutros A, et al. The treatment of advanced melanoma: Current approaches and new challenges. Crit Rev Oncol Hematol. 2024;196:104276.
32. Woodford R, et al. Tumour-infiltrating lymphocyte therapy in melanoma: ready for prime time? Br J Cancer. 2026. https://doi.org/10.1038/s41416-026-03350-z.
33. Centeno PP, Pavet V, Marais R. The journey from melanocytes to melanoma. Nat Rev Cancer. 2023;23:372–90.
34. Garcia-Alvarez A, Ortiz C, Muñoz-Couselo E. Current perspectives and novel strategies of nras-mutant melanoma. Onco Targets Ther. 2021;14:3709–19.
35. Chatziioannou E, et al. Insights into RAS-driven melanoma and its therapeutic implications. Cancer Treat Rev. 2026;143:103090.
36. Hunter MV, et al. Mechanical confinement governs phenotypic plasticity in melanoma. Nature. 2025;647:517–27.
37. Rogava M, et al. Loss of Pip4k2c confers liver-metastatic organotropism through insulin-dependent PI3K-AKT pathway activation. Nat Cancer. 2024;5:433–47.
38. Hebert JD, Neal JW, Winslow MM. Dissecting metastasis using preclinical models and methods. Nat Rev Cancer. 2023;23:391–407.
39. Stribbling SM, Beach C, Ryan AJ. Orthotopic and metastatic tumour models in preclinical cancer research. Pharmacol Ther. 2024;257:108631.

40. Blanchard Z, Brown EA, Ghazaryan A, Welm A. L. PDX models for functional precision oncology and discovery science. Nat Rev Cancer. 2025;25:153–66.
41. Duquet A, et al. A novel genome-wide in vivo screen for metastatic suppressors in human colon cancer identifies the positive WNT - TCF pathway modulators TMED 3 and SOX 12. EMBO Mol Med. 2014;6:882–901.
42. Chen S, et al. Genome-wide CRISPR screen in a mouse model of tumor growth and metastasis. Cell. 2015;160:1246–60.
43. Knott SRV, et al. Asparagine bioavailability governs metastasis in a model of breast cancer. Nature. 2018;554:378–81.
44. Murugaesu N, et al. An in vivo functional screen identifies ST6GalNAc2 sialyltransferase as a breast cancer metastasis suppressor. Cancer Discov. 2014;4:304–17.
45. Sasaki K, et al. Genome-wide in vivo RNAi screen identifies ITIH5 as a metastasis suppressor in pancreatic cancer. Clin Exp Metastasis. 2017;34:229–39.
46. Jin ML, Gong Y, Ji P, Hu X, Shao ZM. In vivo CRISPR screens identify RhoV as a pro-metastasis factor of triple-negative breast cancer. Cancer Sci. 2023;114:2375–85.
47. Hao M, et al. In vivo CRISPR knockout screen identifies p47 as a suppressor of HER2 + breast cancer metastasis by regulating NEMO trafficking and autophagy flux. Cell Rep. 2024;43:113780.
48. Qi Y, Zhang W, Li X, Shi Y, Qu P. A systematic CRISPR screen reveals an NBL1-mediated Jak/Stat3 crosstalk to promote ovarian cancer metastasis. Genes Dis. 2026;13:101740.
49. Scheidmann MC, et al. An In Vivo CRISPR Screen Identifies Stepwise Genetic Dependencies of Metastatic Progression. Cancer Res. 2022;82:681–94.
50. Gobeil S, Zhu X, Doillon CJ, Green MR. A genome-wide shRNA screen identifies GAS1 as a novel melanoma metastasis suppressor gene. Genes Dev. 2008;22:2932–40.
51. Rathore M, et al. Cancer cell-derived long pentraxin 3 (PTX3) promotes melanoma migration through a toll-like receptor 4 (TLR4)/NF-κB signaling pathway. Oncogene. 2019;3:5873–89.
52. Rogava M, et al. Tumor cell intrinsic Toll-like receptor 4 signaling promotes melanoma progression and metastatic dissemination. Int J Cancer. 2022;150:142–51.
53. Hsu RYC, et al. LPS-induced TLR4 signaling in human colorectal cancer cells increases β1 integrin-mediated cell adhesion and liver metastasis. Cancer Res. 2011;71:1989–98.
54. Liao SJ, et al. Triggering of Toll-like receptor 4 on metastatic breast cancer cells promotes αvβ3-mediated adhesion and invasive migration. Breast Cancer Res Treat. 2012;133:853–63.
55. O'Leary DP et al. TLR-4 Signalling Accelerates Colon Cancer Cell Adhesion via NF-κB Mediated Transcriptional Up-Regulation of Nox-1. PLoS ONE 7, (2012).
56. Kawasaki T, Kawai T. Toll-like receptor signaling pathways. Front Immunol. 2014;5:1–8.
57. Jin C, et al. miR-145-5p inhibits tumor occurrence and metastasis through the NF-κB signaling pathway by targeting TLR4 in malignant melanoma. J Cell Biochem. 2019;120:11115–26.

58. Dickinson SE, Wondrak GT. TLR4 in skin cancer: From molecular mechanisms to clinical interventions. Mol Carcinog. 2019;58:1086–93.
59. Luo X, et al. Isolation and Molecular Characterization of Circulating Melanoma Cells. Cell Rep. 2014;7:645–53.
60. Fankhauser R et al. Single-Cell Identification of Melanoma Biomarkers in Circulating Tumor Cells. Cancers (Basel). 14, (2022).
61. Bowley TY, et al. The RPL/RPS Gene Signature of Melanoma CTCs Associates with Brain Metastasis. Cancer Res Commun. 2022;2:1436–48.
62. Hong X, et al. The lipogenic regulator srebp2 induces transferrin in circulating melanoma cells and suppresses ferroptosis. Cancer Discov. 2021;11:678–95.
63. Ward MP, et al. Circulating tumour cells are a prognostic indicator in advanced high-grade serous ovarian cancer and are associated with platelets and immune cells following dissemination. Br J Cancer. 2026;134:22–32.
64. Grigoryeva ES et al. The Association of Integrins β3, β4, and αVβ5 on Exosomes, CTCs and Tumor Cells with Localization of Distant Metastasis in Breast Cancer Patients. Int J Mol Sci 24, (2023).
65. Bolognesi MM, et al. Multiplex Staining by Sequential Immunostaining and Antibody Removal on Routine Tissue Sections. J Histochem Cytochem. 2017;65:431–44.
66. Furia L, et al. Automated multimodal fluorescence microscopy for hyperplex spatial-proteomics: Coupling microfluidic-based immunofluorescence to high resolution, high sensitivity, three-dimensional analysis of histological slides. Front Oncol. 2022;12:1–19.
67. Furia L, Pelicci PG, Faretta M. A computational platform for robotized fluorescence microscopy (II): DNA damage, replication, checkpoint activation, and cell cycle progression by high-content high-resolution multiparameter image-cytometry. Cytometry Part A. 2013;83 A:344–55.
68. Conway T, et al. Xenome-a tool for classifying reads from xenograft samples. Bioinformatics. 2012;28:172–8.
69. Kim D, et al. TopHat2: accurate alignment of transcriptomes in the presence of insertions, deletions and gene fusions. Genome Biol. 2013;14:R36.
70. Love MI, Huber W, Anders S. Moderated estimation of fold change and dispersion for RNA-seq data with DESeq2. Genome Biol. 2014;15:1–21.
71. Huang DW, Sherman BT, Lempicki RA. Systematic and integrative analysis of large gene lists using DAVID bioinformatics resources. Nat Protoc. 2009;4:44–57.
72. Sherman BT, et al. DAVID: a web server for functional enrichment analysis and functional annotation of gene lists (2021 update). Nucleic Acids Res. 2022;50:W216–21.
73. Chen EY et al. Enrichr: Interactive and collaborative HTML5 gene list enrichment analysis tool. BMC Bioinformatics 14, (2013).
74. Kuleshov MV, et al. Enrichr: a comprehensive gene set enrichment analysis web server 2016 update. Nucleic Acids Res. 2016;44:W90–7.

75. Germain PL, Robinson MD, Lun A, Garcia Meixide C, Macnair W. Doublet identification in single-cell sequencing data using scDblFinder. F1000Res. 2022;10:1–26.
76. Qiu X, et al. Reversed graph embedding resolves complex single-cell trajectories. Nat Methods. 2017;14:979–82.

Figures

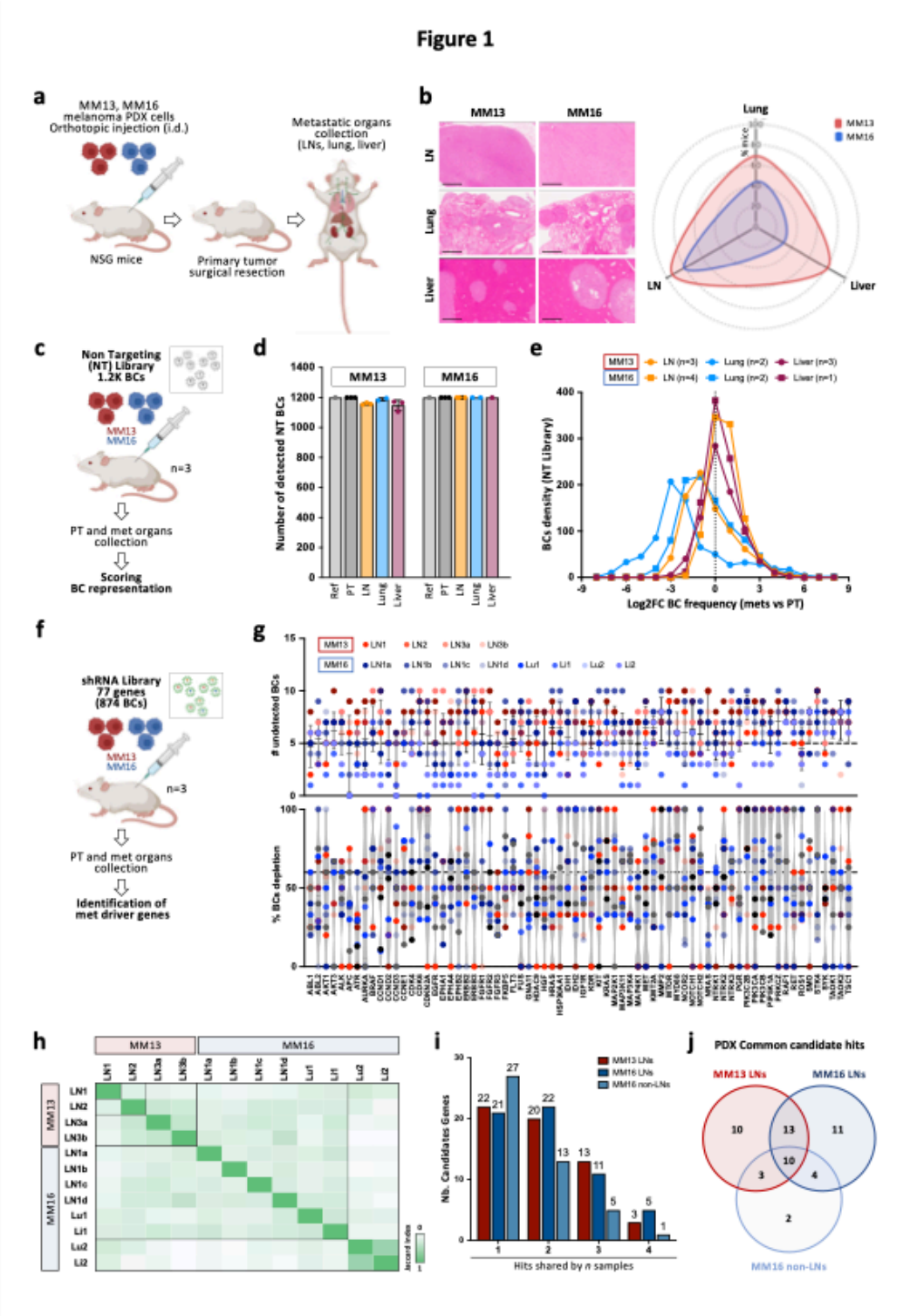


Figure 1

Genetic drop-out screen in NRAS-mutant melanoma PDXs identifies metastasis driver genes: model set-up and feasibility of metastatic screening

Set-up of the PDX model of spontaneous metastasis (**a, b**). **a.** MM13 and MM16 PDX cells (300,000 cells/mouse) were injected intradermally into NSG mice (n=16 *per* PDX). Primary tumors were surgically resected at 300 mm^3 and metastatic organs were subsequently collected. **b.** Metastatic potential of MM13 and MM16 PDXs. Representative hematoxylin and eosin -stained sections of lymph node (LN), lung, and liver samples showing metastatic areas. Scale bar = 1 mm (left). Radar plot showing the percentage of mice with metastases at each site (right).

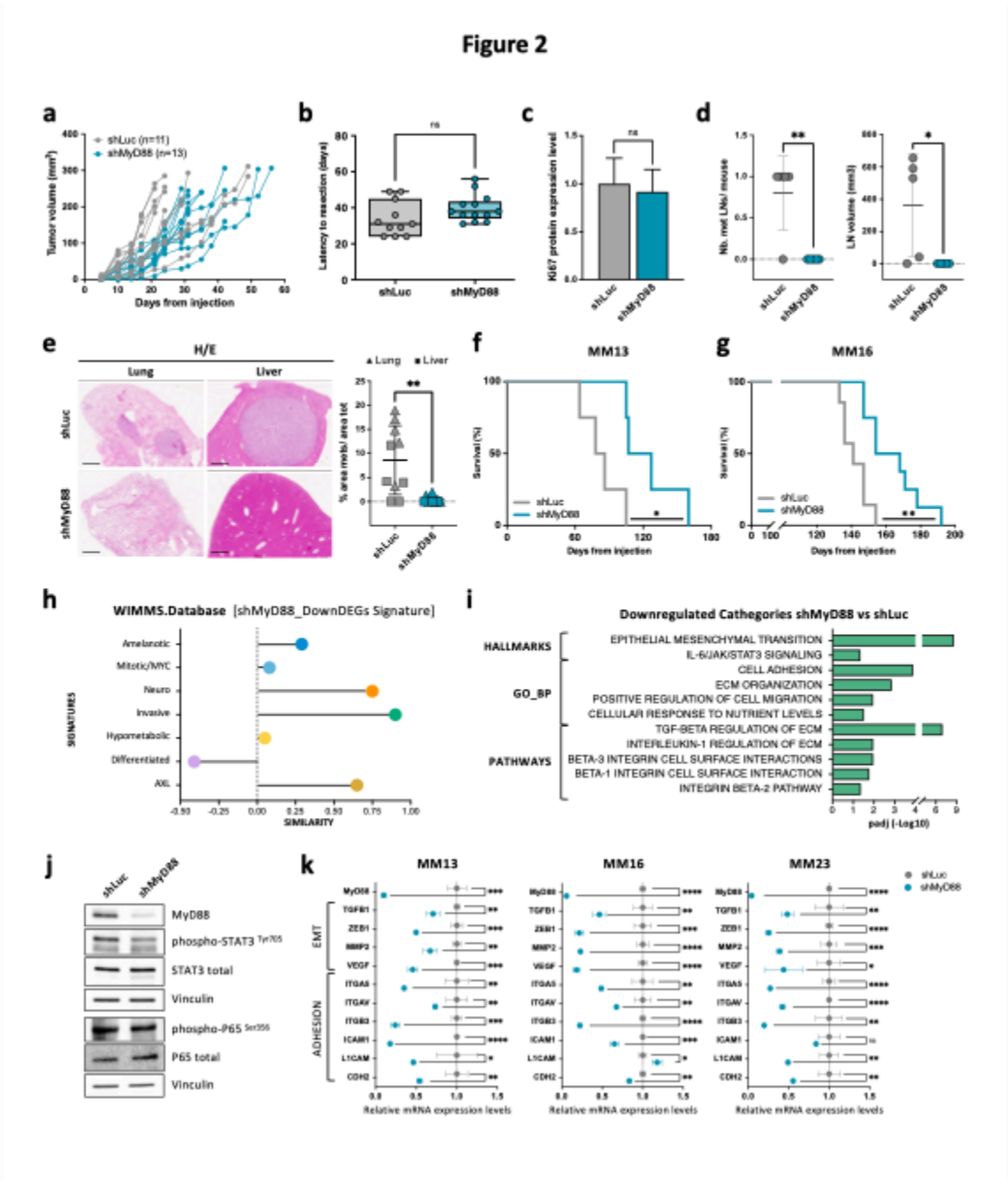


Figure 2

MyD88 silencing reduces the melanoma PDX metastatic behavior by inducing a transcriptional reprogramming toward reversal of the invasive phenotype

Characterization of the role of MyD88 in melanoma progression. Control (shLuc) and MyD88-silenced (shMyD88) MM13/MM16 cells were intradermally injected into NSG mice (300,000 cells/mouse; **a-g**). **a.** MM13 primary tumor growth curves (shLuc, n=11; shMyD88, n=13). **b.** Latency to MM13 tumor resection at 300 mm^3 volume. **c.** Ki67 protein expression levels quantified by immunofluorescence in FFPE sections from MM13 shLuc and shMyD88 primary tumors (n=3). **d.** Number of metastatic LNs *per* mouse (left) and LNs volumes (right), evaluated 90 days after cell injection (MM13, shLuc, n=5 mice; shMyD88, n=5 mice). **e.** Representative hematoxylin and eosin-stained sections of lung and liver tissues from shLuc and shMyD88 MM13 mice (left; scale bar = 1 mm) and quantification of metastatic foci area (right; shLuc, n=5; shMyD88, n=5). **f.** MM13 Kaplan-Meier overall survival curves (shLuc, n=4, median 82 days; shMyD88, n=4, median 117 days). **g.** MM16 Kaplan-Meier overall survival curves (shLuc, n=7, median 141 days; shMyD88, n=8, median 161 days). Bulk RNA sequencing of shLuc and shMyD88 MM13 primary tumors (n=3 tumors; **h-i**). **h.** Downregulated genes in shMyD88 versus shLuc primary tumors (48 genes; Log2FC <-1, adjusted p <0.05) were used to query the WIMMS database and calculate the similarity index among the deposited signatures. **i.** Gene ontology and pathway analysis of downregulated genes (shMyD88 versus shLuc primary tumors) using Enrichr (MSigDB Hallmark 2020) and DAVID Functional Annotation Bioinformatics Resources (GOTERM_BP_DIRECT, KEGG_PATHWAYS). Significantly enriched categories are reported (adjusted p-value <0.05). **j.** Immunoblot analysis of MyD88, phospho- and total STAT3, and phospho- and total NF-κB (p65) in shLuc and shMyD88 MM13 cells. Vinculin was used as a loading control. **k.** Relative RNA expression levels of EMT- and adhesion- related genes evaluated by RT-qPCR in shLuc and shMyD88 MM13, MM16, and MM23 cells (n=3 biological replicates). Data are presented as mean ± SD. P values were calculated using unpaired two-tailed Student's t test (b-e, k) and Log-rank (Mantel-Cox) test (f, g). * p<0.05, ** p<0.01, *** p<0.001, **** p<0.0001; ns, not significant.

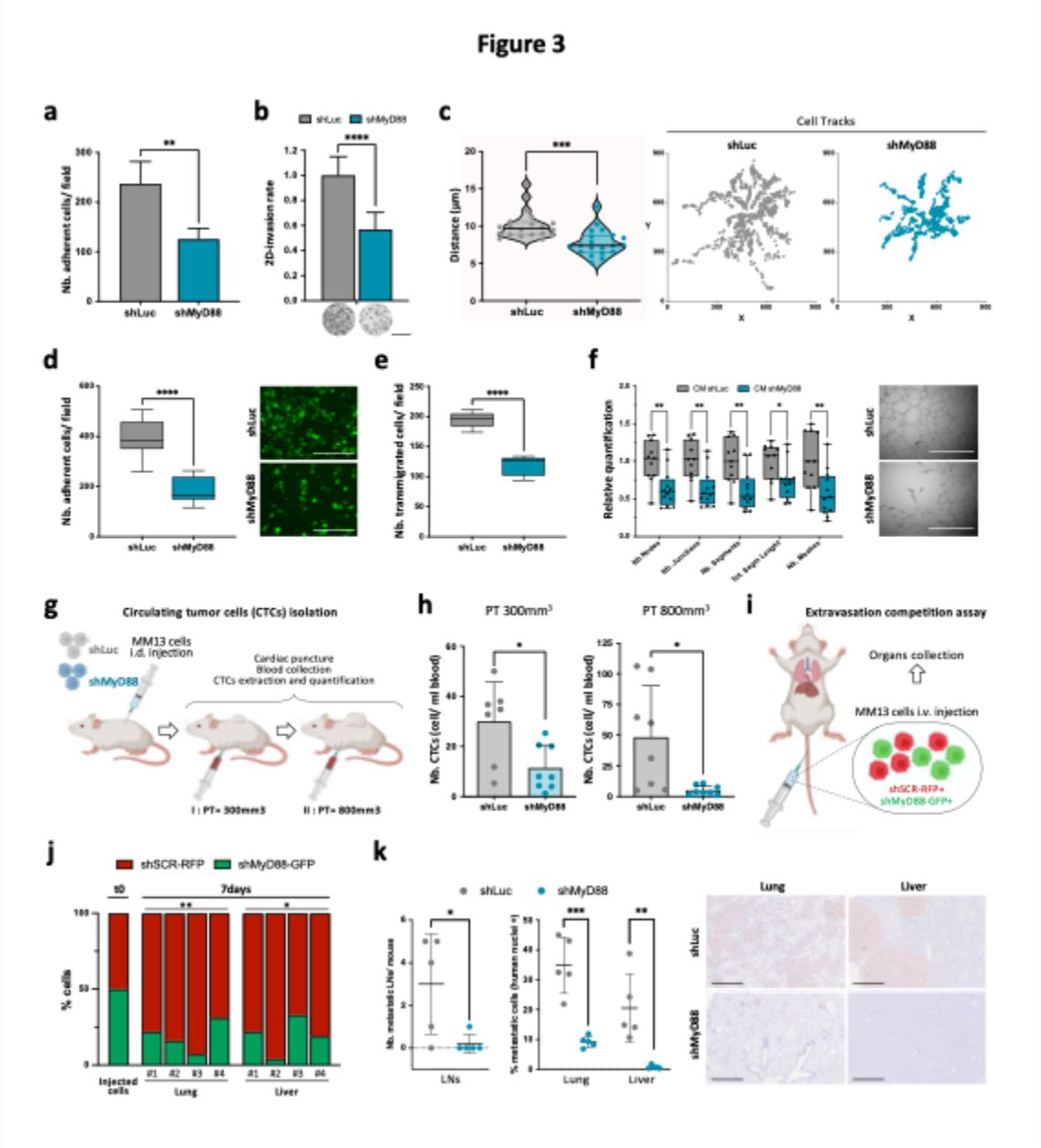


Figure 3

MyD88 drives metastasis by promoting tumor cell adhesion to extracellular matrix and endothelium during intra- and extravasation

In vitro assays characterizing the interaction of shLuc and shMyD88 MM13 cells with extracellular matrix (ECM) and endothelium (**a-f**). **a.** Fibronectin adhesion assay; number of MM13 adherent cells (n=5 images/group from 5 replicate experiments). **b.** Relative 2D-invasion assay of MM13 cells seeded in collagen-coated transwells. Scale bar = 200 µm. (n=8 fields per group from 4 replicate experiments). **c.** Time-lapse analysis of MM13 3D spheroids invasion in collagen; invasion distance by single-cell manual tracking (left) and representative cell tracks (right) (n=20 cells from 2 spheroids/group). **d.** Tumor-endothelial adhesion assay; number of adherent MM13 cells on HMEC1 monolayers. Scale bar = 400 µm. (n=10 field images/group from 5 replicate experiments). **e.** Transendothelial migration assay;

number of MM13 cells migrated through HMEC1 monolayers (n=5 images/group from 5 replicate experiments). **f.** Angiogenic tube formation assay. HMEC1 cells on matrigel were treated with conditioned medium from shLuc or shMyD88 MM13 cells; tube formation parameters (left) and representative images (right). Scale bar = 2000 μm. (n=12 images/group from 3 replicate experiments). Circulating tumor cell (CTC) isolation *in* vivo (**g, h**). **g.** shLuc and shMyD88 MM13 cells (300,000 cells/mouse) were intradermally injected into NSG mice (n=24 mice/group), primary tumors and blood were collected at two time points (300 and 800 mm^3 volume) and CTCs isolated. **h.** Quantification of CTCs at the two time points (n=8 pooled CTCs samples from 12 mice/group). Competition extravasation *in vivo* assay (**i, j**). **i.** A 1:1 mixture of 10^6 shSCR-RFP and 10^6 shMyD88-GFP MM13 cells was injected intravenously into NSG mice (n=4); lung and liver were collected after 7 days. **j.** Relative abundance of fluorescent cells (RFP+ or GFP+) quantified by FACS at t0 (pre-injection) and 7 days. **k.** *In vivo* colonization assay. shLuc and shMyD88 MM13 cells (10^6 cells/mouse) were intravenously injected in NSG mice (n=5); metastatic dissemination was evaluated at 50 days. Representative anti-human nuclei IHC -stained sections of lung and liver (scale bar = 1 mm; left), number of metastatic LNs and percentage of human-nuclei positive cells (right). Data are presented as mean ± SD. P-values were calculated using unpaired two-tailed Student's t test (a-f, h, k) and paired two-tailed Student's t test (j). * p<0.05, ** p<0.01, *** p<0.001, **** p<0.0001.

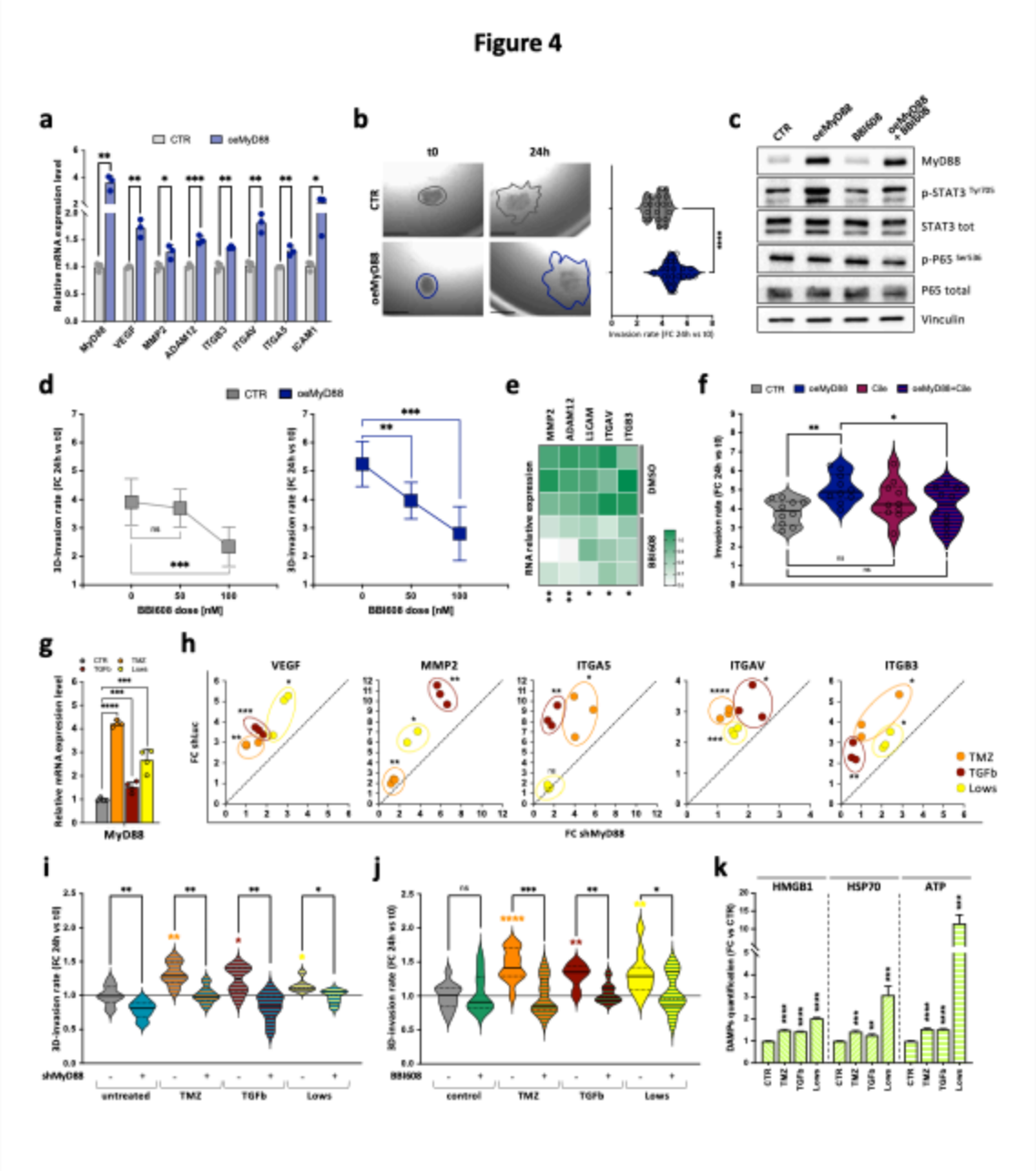


Figure 4

MyD88 overexpression fuels melanoma invasive behavior through a STAT3-dependent program enhanced by environmental stimuli

a. Relative RNA expression levels of EMT- and adhesion- related genes evaluated by RT-qPCR in CTR and oeMyD88 MM13 cells (n=3 biological replicates). **b.** 3D-invasion assay of CTR and oeMyD88 MM13 spheroids embedded in collagen. Invasion rate expressed as the fold change in invaded area at 24h relative to the area at t0. Scale bar = 500 µm. (n=22 spheroids/group). **c.** Immunoblot analysis of MyD88, phospho- and total STAT3, and phospho- and total NF-kB (p65) in CTR and oeMyD88 MM13 cells treated with vehicle (DMSO) or BBI608 (500nM, 4h). Vinculin was used as a loading control. **d.** 3D-invasion assay of CTR and oeMyD88 MM13 spheroids embedded in collagen, treated with BBI608 (0-50-100nM) (CTR,

n=11-13; oeMyD88, n=7-9 spheroids). **e.** Relative RNA expression levels of EMT- and adhesion- related genes evaluated by RT-qPCR in vehicle (DMSO) or BBI608-treated (500nM for 4h) MM13 cells (n=3 biological replicates). **f.** 3D-invasion assay of CTR and oeMyD88 MM13 spheroids embedded in collagen, treated with cilengitide (1μM for 24h) (n=10 spheroids per group). **g.** Relative MyD88 RNA expression levels evaluated by RT-qPCR in untreated (CTR) and stimuli-treated (temozolomide, TMZ, 10μM; TGFb, 25ng/ml; Lows, 3% serum and 3%oxygen) MM13 cells (n=4 biological replicates). **h.** Relative RNA expression levels of EMT- and adhesion- related genes evaluated by RT-qPCR in shLuc and shMyD88 MM13 cells exposed to stimuli and normalized to the corresponding untreated sample (n=3 biological replicates). **i.** 3D-invasion assay of shLuc and shMyD88 -transduced MM13 spheroids embedded in collagen, untreated or stimuli-treated (TMZ, 20μM; TGFb, 50ng/ml; Lows, 3% serum and 3% oxygen; n=6-10 spheroids/group). **j.** 3D-invasion rate of MM13 spheroids embedded in collagen, untreated or treated with BBI608 (50nM) and/or stimuli (n=8-12 spheroids/group). **k.** Quantification of released DAMPs (HMGB1, HSP70, ATP) in untreated and stimuli-treated MM13 cells; values are normalized to CTR levels (n=3 biological replicates). Data are presented as mean ± SD. P-values were calculated using unpaired two-tailed Student's t test (a-b, d-k). * p<0.05, ** p<0.01, *** p<0.001, **** p<0.0001; ns, not significant.

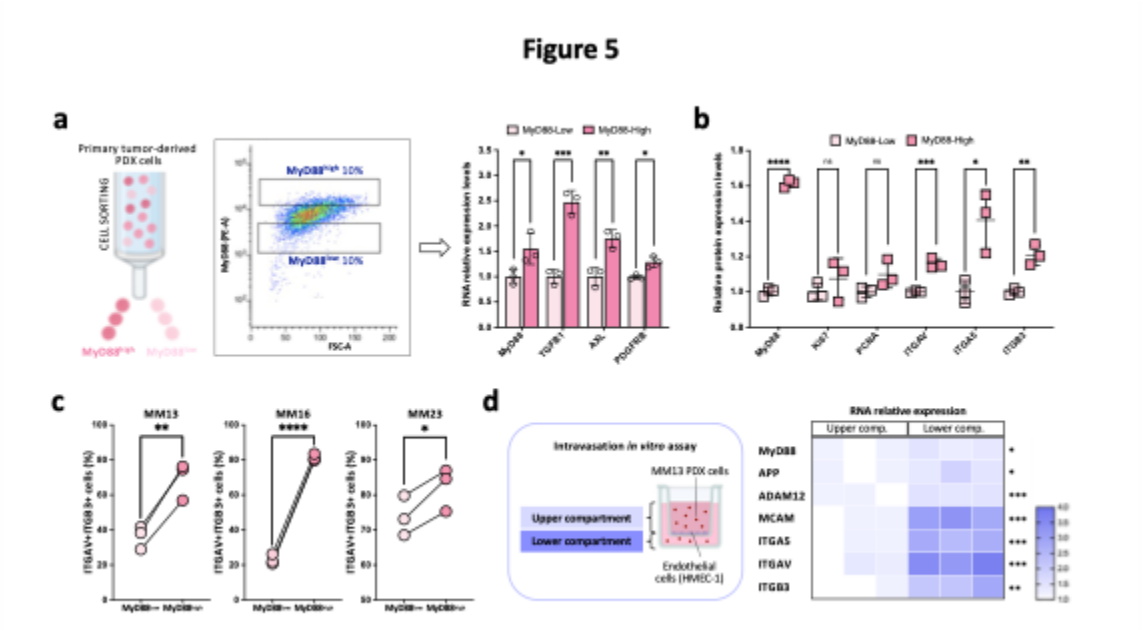


Figure 5

MyD88 heterogeneity associates with invasive and integrin-related features

a. MM13 PDX primary tumor-derived cells are FACS-sorted based on MyD88 expression. Representative plot (left) and relative RNA expression levels of EMT-related genes evaluated by RT-qPCR, in MyD88^{high} and MyD88^{low} MM13 cells (right) (n=3 biological replicates). **b.** Relative protein expression levels evaluated by multiplexing immunofluorescence on MM13 primary tumor FFPE sections (n=3 mice). **c.** Percentage of double positive ITGAV+ITGB3+ cells evaluated by flow cytometry in gated MyD88^{high} and

MyD88^{low} MM13, MM16, and MM23 cells (n=3 biological replicates). **d.** Trans-endothelial migration assay. MM13 cells were separately collected from the upper and lower compartments 16h after seeding (left) and relative RNA expression levels of EMT- and adhesion-related genes were evaluated by RT-qPCR (right) (n=3 biological replicates). Data are presented as mean ± SD. P-values were calculated using unpaired two-tailed Student's t test (a, b, d) and paired two-tailed Student's t test (c). * p<0.05, ** p<0.01, *** p<0.001, **** p<0.0001; ns, not significant.

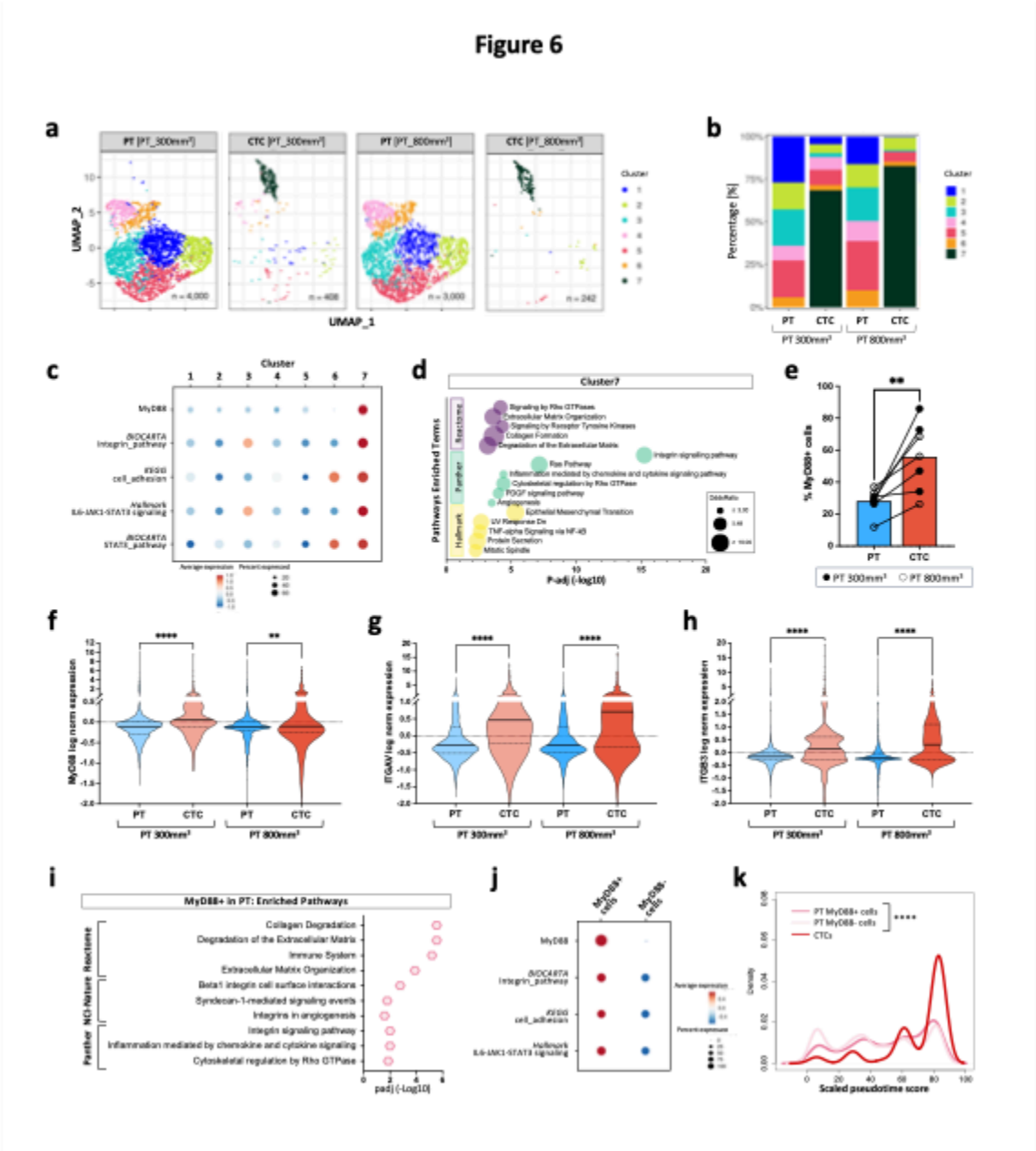


Figure 6

Cells with high MyD88 expression are positively selected throughout the metastatic cascade

Single-cell RNA sequencing of MM13 primary tumors and circulating tumor cells (CTCs). MM13 cells (300,000 cells/mouse) were injected intradermally into NSG mice (n=24 mice), and PT and blood were collected at two time points (300-800 mm^3 tumor volume). PTs and isolated CTCs were subjected to single-cell RNA sequencing (n=3-4 pooled samples from 12 mice *per* time point; **a-h**). **a.** UMAP visualization of cell clustering; each dot represents a single cell colored by cluster identity. **b.** Relative distribution of cells across clusters. **c.** Dot plot showing the expression of MyD88 and selected signatures across clusters. **d.** Pathways analysis of cluster7 based on the top 200 marker genes ranked by adjusted p-value, using Reactome 2024, Panther 2016, MSigDB Hallmarks 2020. Displayed pathways were selected for their relevance among the top-ranking 13 enriched terms. **e.** Percentage of MyD88+ cells (reads>0) in PT and CTCs. **f-h.** Violin plot showing expression levels of MyD88 (F), ITGAV (G), and ITGB3 (H) in PT and CTCs. **i.** Pathway analysis showing enriched categories in MyD88+ cells in PT (top 26 marker genes ranked by adjusted p-value; log2FC>1.1; Reactome 2024, NCI-Nature, Panther 2016). **j.** Dot plot of the expression of MyD88 and selected signatures in MyD88+ and MyD88- cells in PT. **k.** Density plot of trajectory analysis of PT (MyD88+ and MyD88- cells) and CTCs. Data are presented as mean ± SD. P-values were calculated using paired two-tailed Student's t test (e), Mann-Whitney test (f-h), and Wilcoxon test (K). * p<0.05, ** p<0.01, *** p<0.001, **** p<0.0001; ns, not significant.

Figure 7

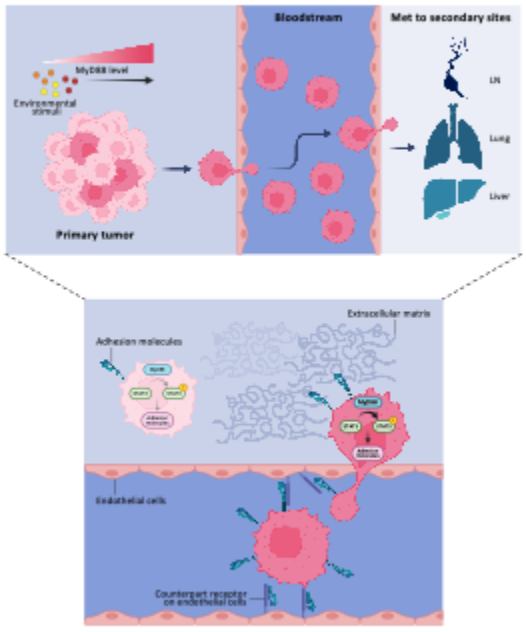


Figure 7

MyD88 integrates environmental stimuli to activate STAT3-dependent adhesion programs that sustain metastasis-competent melanoma cell states and promote dissemination.

Supplementary Files

This is a list of supplementary files associated with this preprint. Click to download.

- SupplementaryFigures.pdf
- SupplementaryTable1.xlsx
- SupplementaryTable4.xlsx
- SupplementaryTable7.xlsx
- SupplementaryTable2.xlsx
- SupplementaryTable5.xlsx
- SupplementaryTable3.xlsx
- SupplementaryTable6.xlsx
- UncroppedBlots.pdf